

Spectroscopic Evidence of Competing Diagonal Spin Interactions and Spin Disproportionation in the Bilayer Nickelate $\text{La}_3\text{Ni}_2\text{O}_7$

Dong-Hyeon Gim,¹ Dirk Wulferding,² Hengyuan Zhang,³ Meng Wang,³ and Kee Hoon Kim^{1,4,*}

¹*Department of Physics and Astronomy, Seoul National University, Seoul 08826, Korea*

²*Department of Physics and Astronomy, Sejong University, Seoul 05006, Korea*

³*Institute of Neutron Science and Technology, Guangdong Provincial Key Laboratory of Magnetolectric Physics and Devices, School of Physics, Sun Yat-Sen University, Guangzhou, Guangdong 510275, China*

⁴*Institute of Applied Physics, Seoul National University, Seoul 08826, Korea*

**Contact author: optopia@snu.ac.kr*

ABSTRACT

A comprehensive spectroscopic map of the electronic, magnetic, and lattice excitations is presented for the bilayer nickelate $\text{La}_3\text{Ni}_2\text{O}_7$ using Raman scattering at ambient pressure. Upon entering the spin density wave state below 153 K, the A_{1g} channel exhibits an abrupt electronic spectral gap with a clear isosbestic point. In contrast, the B_{1g} and B_{2g} channels are dominated by pronounced two-magnon (2M) excitations, representing an unambiguous signature of incipient Mottness. These 2M signals in both channels constitute direct evidence for two distinct in-plane spin exchange interactions along the Ni-O bonding and its diagonal directions. Calculations based on the spin wave theory further reveal that the 2M mode in the B_{2g} channel arises from the competition between two bond-diagonal antiferromagnetic interactions mediated by nickel $d_{x^2-y^2}$ orbitals. Furthermore, emergent low-energy 2M excitations below 10 meV are found to originate from distinct, weaker spin moments, strongly supporting spin disproportionation. Simultaneously, an anomalous softening of B_{1g} phonons from 280 down to 4.5 K is uncovered, suggesting the presence of an incipient lattice instability leading to checkerboard-type breathing modulations. Collectively, these findings identify a ground state of the bilayer nickelate characterized by competing bond-diagonal interactions, spin disproportionation, and an incipient lattice instability, establishing key ingredients for understanding the mechanism of nickelate superconductivity.

I. INTRODUCTION

The discovery of pressure-induced high-temperature superconductivity (SC) in the bilayer nickelate $\text{La}_3\text{Ni}_2\text{O}_7$ with a critical temperature as high as $T_c = 80$ K [1] has sparked intense interest in the mechanisms of unconventional SC. Given that $\text{La}_3\text{Ni}_2\text{O}_7$ exhibits a spin density wave (SDW) transition at lower pressures [2,3], the interplay between the SDW and SC is expected to be crucial, which has motivated numerous theoretical proposals explaining the intertwined ground states based on the SDW and SC. However, the nature of SC in $\text{La}_3\text{Ni}_2\text{O}_7$ remains a subject of intense debate. Theories based on various models have led to divergent scenarios on the possible pairing mechanism [4–20]. Experimentally, investigations on the pressurized crystals and strained films have resulted in conflicting interpretations regarding whether the primary SC gap symmetry is a fully gapped *s*-wave or a nodal *d*-wave [21–23]. Given that the emergence of SC is intimately linked to the underlying electronic and magnetic correlations, understanding the parent SDW state provides an important foundation for elucidating the SC mechanism.

Nevertheless, beyond its ordering vector $\mathbf{Q}_{\text{SDW}} = (\pi/2, \pi/2, 0)$ [3], the exact spin configuration of the SDW state remains controversial. Although the magnon dispersion measurements by resonant inelastic x-ray scattering (RIXS) have revealed sizable interlayer (J_c) and secondary intralayer (J_3) spin interactions [24], the resulting spin pattern—whether spin-charge or double-spin stripes—is undetermined. An inelastic neutron scattering (INS) study could not detect signatures of a long-range spin ordering, presumably because magnetic moments were too weak [25]. Meanwhile, the muon spin rotation and relaxation (μSR) and neutron powder diffraction (NPD) studies suggested the coexistence of two nickel spin moments ($m_1 = 0.66$ and $m_2 = 0.05\mu_B$) [3,26]. In contrast, an x-ray absorption spectroscopy (XAS) and x-ray scattering study on the $\text{La}_3\text{Ni}_2\text{O}_7$ films concluded a double-spin stripe pattern without such spin or charge disproportionation where nickel spins are aligned in the plane, being perpendicular to \mathbf{Q}_{SDW} [27]. Moreover, a nuclear magnetic resonance study suggested rather a small but uniform out-of-plane spin moments of $\sim 0.1\mu_B$, supporting the double-spin stripe pattern [28]. On the other hand, a nuclear quadrupolar resonance study raised the possibility of coexisting charge density wave (CDW) states, adding another layer of complexity [29].

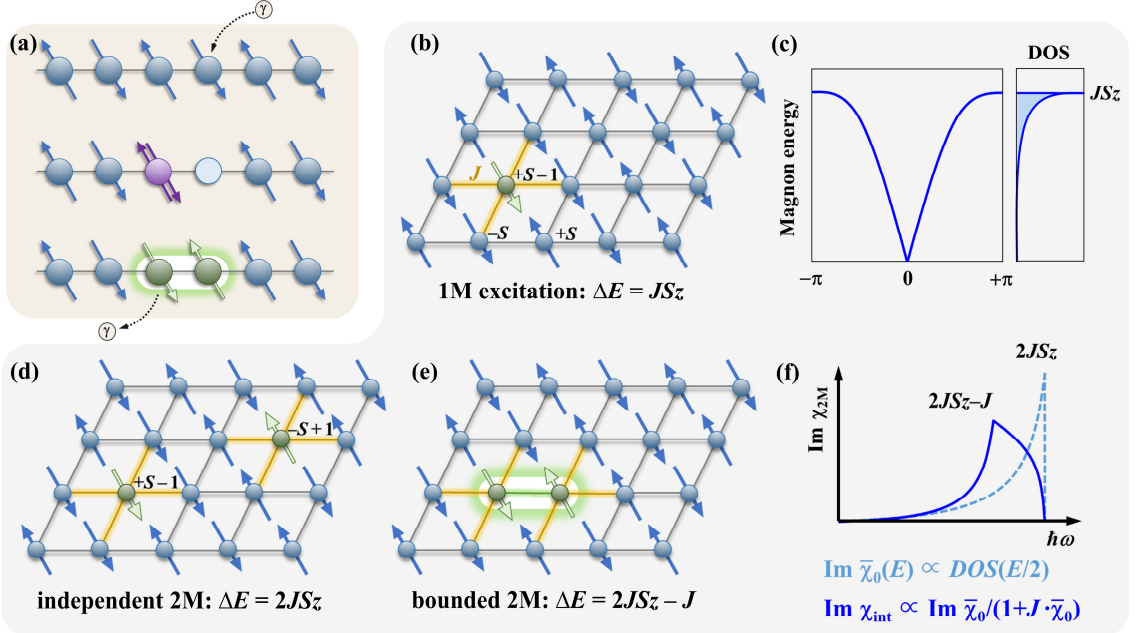


FIG. 1. Raman scattering process of 2M excitations. (a) The Fleury-Loudon exchange-scattering mechanism in antiferromagnets. An incident photon (γ) virtually excites an electron to a neighboring site; the subsequent exchange process creates two adjacent, opposite spin-flips in the final state. (b)-(f) Energy costs of spin-flips. z is the number of nearest neighbors. Single 1M spin-flip (b) spectrum peaks at JS_z [(c), right panel]. Spectrum of a distant, non-interacting 2M excitation (d) peaks at $2JS_z$ [(f), dashed line]. Renormalized spectrum of an adjacent, interacting 2M excitation (e) peaks at a lower energy shifted by J [(f), solid line].

The conflicting interpretations from various experiments have precluded a coherent understanding of the electronic and magnetic properties of $\text{La}_3\text{Ni}_2\text{O}_7$. To elucidate the essential microscopic interactions in $\text{La}_3\text{Ni}_2\text{O}_7$, we employ comprehensive, symmetry-resolved Raman spectroscopy (see Appendix A for experimental details). Raman scattering is uniquely sensitive to antiferromagnetic (AF) spin-flip processes, specifically two-magnon (2M) excitations (Fig. 1), which are governed by the Fleury-Loudon (FL) exchange scattering mechanism [30]. The corresponding scattering Hamiltonian, which depends on the incident ($\hat{\mathbf{e}}_I$) and scattered ($\hat{\mathbf{e}}_S$) light polarizations, is given by:

$$\mathcal{H}_{\text{FL}} = \sum_{\langle i,j \rangle} J_{ij} (\hat{\mathbf{e}}_I \cdot \hat{\mathbf{r}}_{ij})(\hat{\mathbf{e}}_S \cdot \hat{\mathbf{r}}_{ij}) \mathbf{S}_i \cdot \mathbf{S}_j, \quad (1)$$

where J_{ij} is the exchange interaction between spins \mathbf{S}_i and \mathbf{S}_j on sites i and j , and $\hat{\mathbf{r}}_{ij}$ is the unit vector connecting them. As Eq. (1) demonstrates, the Raman selection rules

establish a direct link between the polarization configuration ($\hat{\mathbf{e}}_I \hat{\mathbf{e}}_S$) and the geometry of magnetic bonds. Consequently, the 2M Raman response provides energy- and symmetry-dependent constraints on the spin interactions in antiferromagnets [31–41], which are crucial for determining the magnetic ground states.

II. RESULTS

Figures 2(a)-(c) present the phonon-subtracted $\text{La}_3\text{Ni}_2\text{O}_7$ Raman response ($\text{Im } \tilde{\chi}$) measured in three polarization configurations: (LL), ($y'x'$), and (xy). Here, L denotes left circularly polarized light, x and y represent linear polarizations parallel to the in-plane tetragonal axes, and x' and y' are rotated by 45° (details on crystal orientation and phonon subtraction are provided in Appendices A and B). Within the quasi-tetragonal D_{4h} description, these scattering geometries selectively probe excitations in the A_{1g} (s -wave), B_{1g} ($d_{x^2-y^2}$ -wave), and B_{2g} (d_{xy} -wave) symmetry channels, respectively (Appendix C). Across all three symmetry channels, the Raman response exhibits a pronounced temperature evolution depending on the energy $\hbar\omega$.

Upon cooling below the SDW transition temperature $T_{\text{SDW}} = 153$ K, the A_{1g} channel exhibits a clear signature of an electronic gap opening with the resulting isosbestic point near 50 meV [Fig. 2(a)]: While the low-energy spectral weight (SW) below 50 meV remains nearly constant above T_{SDW} , it is sharply suppressed below T_{SDW} , depleted to a value close to zero. The low-energy dynamic susceptibility difference $\Delta\tilde{\chi}_0(T) = \int_{3 \text{ meV}}^{50 \text{ meV}} d\hbar\omega \text{Im}[\tilde{\chi}(T) - \tilde{\chi}(280 \text{ K})]/\hbar\omega$ integrated up to the isosbestic point also decreases sharply below T_{SDW} [green circles in Fig. 2(d)], corroborating the gap opening behavior. Notably, the electronic SDW gap in the trilayer nickelate $\text{La}_4\text{Ni}_3\text{O}_{10}$ also develops most prominently in the A_{1g} Raman channel [42]. This suggests that the SDW formation in both bilayer and trilayer nickelates may involve similar electronic reconstructions, leaving a fingerprint in the four-fold symmetric scattering channel.

In contrast, the SWs in the B_{1g} and B_{2g} channels show complex behaviors starting well above T_{SDW} [Figs. 2(d),(e)], driven by the high-energy peaks located above 40 meV (see Appendix D for detailed analysis). Furthermore, as T drops below 30 K, distinct low-energy humps emerge below 15 meV in both the B_{1g} and B_{2g} channels [insets of Figs. 2(b),(c)].

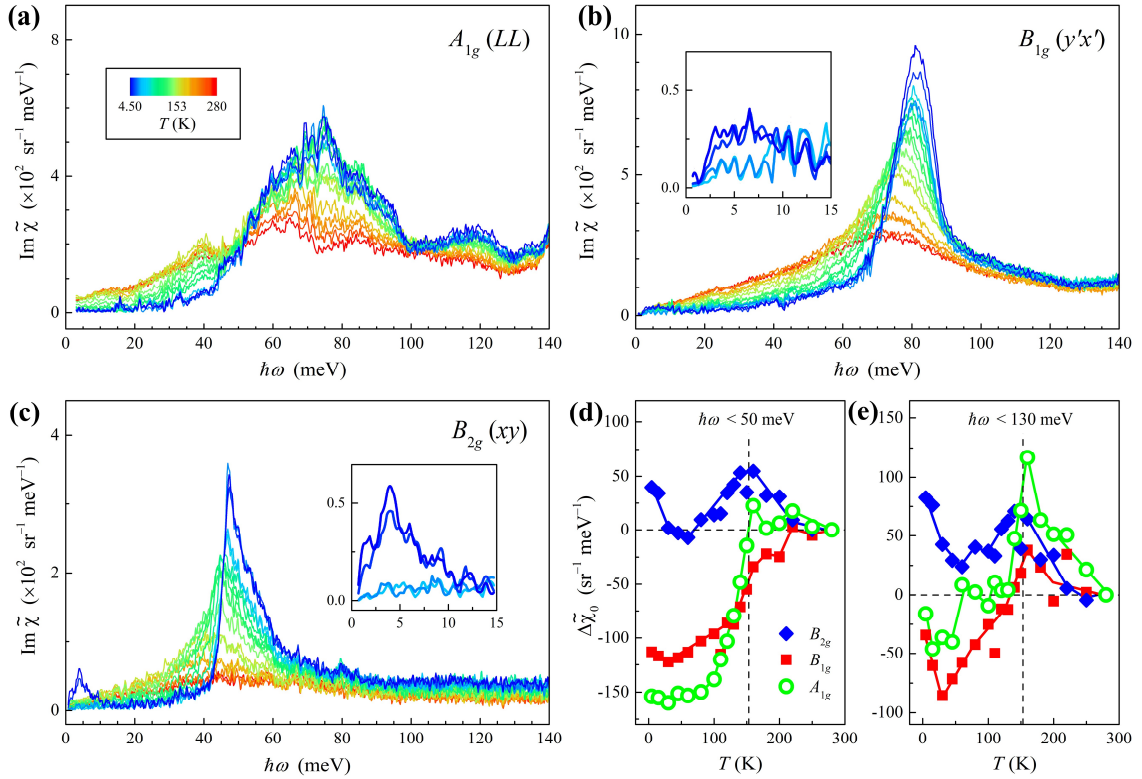


FIG. 2. Temperature-dependent Raman response of $\text{La}_3\text{Ni}_2\text{O}_7$. (a)-(c) Phonon-subtracted Raman response in the A_{1g} (LL), B_{1g} ($y'x'$), and B_{2g} (xy) symmetry channels, respectively. Insets in (b),(c) show the low-energy region at 4.5, 15, 30, and 45 K. (d),(e) SW difference $\Delta \tilde{\chi}_0$ in each scattering channel is integrated up to 50 and 130 meV, respectively. Solid lines are guides for the eye. Vertical dashed lines represent T_{SDW} .

III. MULTICHANNEL SPIN-EXCHANGE EXCITATIONS

The prominent peaks in the B_{1g} and B_{2g} channels are characteristic signatures of 2M excitations generated by two opposite spin-flips at adjacent sites (Fig. 1; Appendix D). The simultaneous observation of the prominent 2M peaks in both B_{1g} and B_{2g} channels marks a key feature distinguishing $\text{La}_3\text{Ni}_2\text{O}_7$ from cuprate superconductors. In cuprates, the nearest-neighbor exchange interaction J_1 is dominant, generating 2M peaks near $3.6J_1$ exclusively in the B_{1g} channel [36,37]. In contrast, the magnetic B_{2g} response in cuprates appears only as a much broader and weaker feature at a higher energy, originating from higher-order processes involving itinerant charge carriers or quantum fluctuations [36,43].

In sharp contrast, in $\text{La}_3\text{Ni}_2\text{O}_7$, the B_{2g} signal is detected as a sharp peak with substantial intensity (approximately 37% of the B_{1g} intensity), and its peak energy (47 meV at 4.5 K) is even lower than that of the B_{1g} peak (81 meV). These observations

strongly indicate that the B_{1g} and B_{2g} peaks in $\text{La}_3\text{Ni}_2\text{O}_7$ arise from the same fundamental mechanism, i.e., the FL exchange scattering process of 2M excitations. As evident from Eq. (1), the 2M signal in the B_{1g} (B_{2g}) channel is generated by the exchange interactions along the tetragonal axes (diagonal directions) [Fig. 3(a)]. The observation of strong 2M signals in both channels therefore provides direct evidence for the presence of significant exchange interactions (i.e., J_3 and $J_{2a,b}$) in $\text{La}_3\text{Ni}_2\text{O}_7$ along the Ni-O bonding and its diagonal directions.

To verify whether the observed Raman signals originate from the 2M excitations, we calculate the 2M Raman response using parameters listed in Table I, incorporating the high (m_1) and low (m_2) spin moments consistent with the recent μSR and NPD studies [3,26]. We first compute the non-interacting 2M density of states (DOS) spectra, $\text{Im } \bar{\chi}_0$, based on the \mathbf{k} -dependent magnon energies and the corresponding scattering matrix elements derived from Eq. (1) [Fig. 3(b)]. The final interacting response ($\text{Im } \chi_{\text{int}}$) is then obtained by applying a random phase approximation (RPA)-type renormalization that accounts for magnon-magnon interactions [Figs. 1(e),(f)] [31,32,35,44,45]:

$$\text{Im } \chi_{\text{int}} \propto \text{Im } \frac{\bar{\chi}_0}{1 + J_\alpha \cdot \bar{\chi}_0}. \quad (2)$$

Here, J_3 and J_{2a} are used for the interaction vertex J_α in the B_{1g} and B_{2g} channels, respectively. The full theoretical procedures are outlined in Appendix E.

TABLE I. Parameters used for the 2M calculation. Magnetic moments and exchange interactions given in units of μ_B and meV, respectively. $S_1 = m_1/g\mu_B = 0.33$ with a g -factor of 2.

m_1	m_2	$J_c S_1$	$J_{2a} S_1$	$J_{2b} S_1$	$J_3 S_1$
0.66	0.033	52.8	1.98	0.99	4.62

The calculated bare and renormalized spectra are presented in Fig. 3(c) and compared with the experimental data at 4.5 K. Notably, the theoretical results successfully reproduce the key experimental features, i.e., the peak energies, the overall lineshapes, and even the relative intensities of the B_{1g} and B_{2g} signals. This close agreement validates our assignment of the B_{1g} and B_{2g} features to the 2M excitations and, in turn, confirms the presence of significant in-plane exchange interactions along both the bonding and diagonal directions.

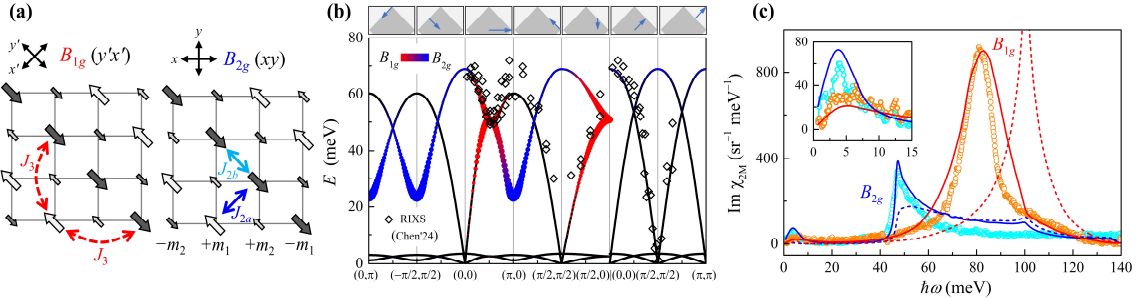


FIG. 3. 2M excitations and multichannel exchange interactions. (a) Schematic of the magnetic structure and exchange interactions probed in each symmetry channel. (b) Calculated magnon dispersion relations (lines) using parameters from Table I, compared with the RIXS data (squares) [24]. Color scale indicates the calculated strength of Raman scattering matrix elements for the B_{1g} (red) and B_{2g} (blue) channels. (c) Calculated bare (dashed) and renormalized (solid lines) 2M response in the B_{1g} (red) and B_{2g} (blue) channels are compared with the experimental data at 4.5 K (orange and cyan circles). For this comparison, we subtracted a small high-energy background, assuming quadratic energy dependence, from the B_{1g} data [Fig. 2(b)]. Inset: a magnified view below 15 meV, showing features arising from the low-moment ($\pm m_2$) sublattices.

These results constitute first, direct spectroscopic evidence for two distinct intralayer exchange interactions: J_3 along the Ni-O bond direction and $J_{2a,b}$ along the diagonal. J_3 is a superexchange interaction between high-moment (m_1) sites mediated by an intervening low-moment (m_2) site, while $J_{2a,b}$ represents a direct π -hopping exchange between nickel $d_{x^2-y^2}$ orbitals [46]. Our observations therefore highlight the crucial role of $d_{x^2-y^2}$ orbitals on the intralayer interaction in forming the SDW ground state, complementing the dominant interlayer magnetic coupling (J_c) mediated by $d_{3z^2-r^2}$ orbitals. This significant spin exchange along the diagonal directions has not been directly identified by previous RIXS and INS studies [24,25]. Importantly, the presence of bond-diagonal spin exchange interactions marks a key distinction between the magnetism of $\text{La}_3\text{Ni}_2\text{O}_7$ and that of the cuprates. Furthermore, the presence of these prominent 2M modes distinguishes $\text{La}_3\text{Ni}_2\text{O}_7$ from other layered nickelates such as $\text{La}_4\text{Ni}_3\text{O}_{10}$ where such features are much weaker [42], indicating that $\text{La}_3\text{Ni}_2\text{O}_7$ is positioned far closer to the localized, Mott-insulating limit [40,41].

In addition, our analysis reveals that a competition between two distinct diagonal AF interactions is essential to the magnetism in $\text{La}_3\text{Ni}_2\text{O}_7$. To reproduce the lineshape of the high-energy B_{2g} 2M peak, the model requires two diagonal AF interactions: J_{2a}

between the opposite magnetic sublattices and J_{2b} within the same sublattice [Fig. 3(a)]. As demonstrated in Appendix E, if J_{2b} is absent or ferromagnetic, it fails to reproduce the observed B_{2g} spectrum. Furthermore, the magnetic structure with \mathbf{Q}_{SDW} becomes unstable if $J_{2a} < J_{2b}$. Consequently, in order to consistently reproduce the relative 2M spectra while preserving the stability of the reported \mathbf{Q}_{SDW} , our calculations constrain J_{2a} to be approximately twice as large as J_{2b} .

The presence of competing diagonal AF interactions provides a natural explanation for stabilizing spin-stripe order at low pressures and has profound implications for the high-pressure tetragonal phase where SC emerges. In the low-pressure orthorhombic phase, the lattice distortion lifts the degeneracy of the two diagonal directions ($x' \neq y'$). The resulting imbalance between J_{2a} and J_{2b} allows a uniaxial AF stripe pattern propagating along the diagonal direction determined by the stronger AF interaction path. In the high-pressure tetragonal phase, the orthorhombic distortion vanishes so that J_{2a} and J_{2b} should become equivalent. Given that the on-axis interaction (J_3) likely remains dominant, the presence of two degenerate and competing diagonal AF interactions in the tetragonal phase is expected to induce strong in-plane spin frustration, which could result in significant spin fluctuations and potentially destabilize long-range stripe order.

IV. COLLECTIVE LOW-ENERGY MAGNETIC MODES

Beyond the prominent high-energy 2M peaks, we identify distinct features emerging below 10 meV in the B_{1g} and B_{2g} spectra at $T < 30$ K [insets of Figs. 2(b),(c)]. These features are reproduced by our theoretical model [Fig. 3(c) inset], corresponding to 2M excitations originating from the low-energy magnon branches below 5 meV in the spin wave dispersion [Fig. 3(b)]. Crucially, these low-energy 2M peaks vanish in the calculations if we assume either an ideal spin-charge stripe ($m_2 = 0$) or a simple double-spin stripe with uniform moments ($m_2 = m_1$), both of which have been recently considered as a possible ground state configuration [24] (see the additional calculation results in Appendix E). Therefore, the observation of the 2M excitations below 10 meV constitutes unambiguous spectroscopic evidence for small but finite low-spin moments, corroborating the recent suggestions from the NPD and μ SR analyses [3,26]. By unveiling

these symmetry-specific, collective excitations, our results demonstrate that the double-spin stripe with a nonuniform spin moment distribution ($m_1 \approx 20m_2 \approx 0.66\mu_B$) is the true spin ground state in $\text{La}_3\text{Ni}_2\text{O}_7$.

The assignment of the low-energy feature to the 2M excitations arising from the low-moment magnetic sublattices aligns with the RIXS and XAS reports indicating mixed $d^8 + d^8\underline{L} + d^7$ valence states (\underline{L} denotes ligand holes) in $\text{La}_3\text{Ni}_2\text{O}_7$ [24]. Note that the mixed valence state in the perovskite nickelates is known as the origin of mixed spin states (i.e., spin disproportionation) [47]. Based on these converging results, we conclude that our spectroscopic data provide firm evidence for spin disproportionation in the magnetic structure of $\text{La}_3\text{Ni}_2\text{O}_7$. As a result, the system exhibits two distinct spin moments, with the weaker moment being approximately an order of magnitude smaller than the stronger one.

V. INCIPEINT LATTICE INSTABILITY

As summarized in Figs. 4(a)-(g), the phonon modes in $\text{La}_3\text{Ni}_2\text{O}_7$ exhibit distinct temperature dependence. While most optical phonons display conventional anharmonic hardening upon cooling [Fig. 4(c); Appendix B], several modes exhibit anomalies clearly linked to the magnetic transition. For instance, the $B_{1g}^{(6)}$ mode initially hardens at high temperatures before softening below T_{SDW} [Fig. 4(d)], and certain A_{1g} phonons (e.g., $A_{1g}^{(11)}$ and $A_{1g}^{(16)}$) display kinks in their temperature dependence at T_{SDW} (Appendix B). This behavior is characteristic of spin-phonon coupling present in $\text{La}_3\text{Ni}_2\text{O}_7$, by which the onset of the long-range magnetic order modifies the lattice dynamics.

Notably, we observe that low-energy $B_{1g}^{(1)}$ and $B_{1g}^{(2)}$ phonons soften continuously upon cooling starting far above T_{SDW} [Figs. 4(a),(b)]. This softening is particularly dramatic for the $B_{1g}^{(1)}$ mode, whose energy decreases smoothly across the SDW transition. The total amount of this energy reduction exceeds 1.5 meV, which is over 25% of its phonon frequency at room temperature (~ 6 meV) and an order of magnitude larger than the shifts in other phonons. The magnitude of this softening, combined with its insensitivity to the magnetic ordering, indicates that this phenomenon

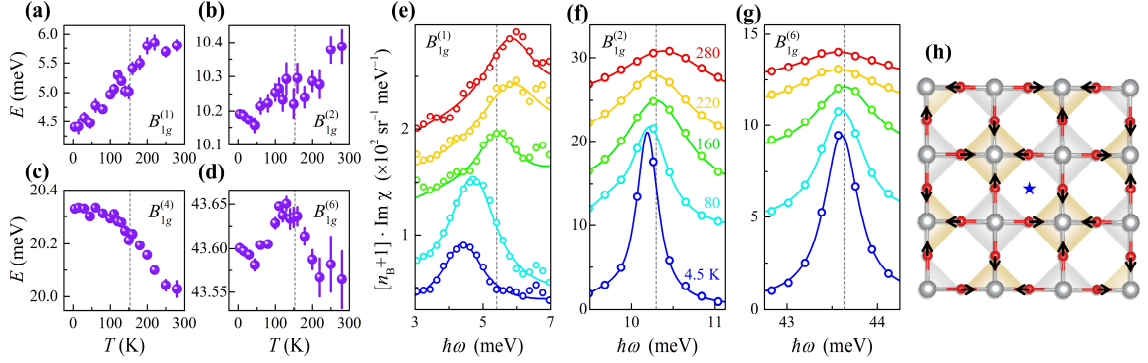


FIG. 4. Soft B_{1g} phonons. (a)-(d) Temperature-dependent energies of $B_{1g}^{(1)}$, $B_{1g}^{(2)}$, $B_{1g}^{(4)}$, and $B_{1g}^{(6)}$ phonons. Vertical dashed lines indicate T_{SDW} . Data for other phonons are shown in Fig. 7. (e)-(g) Raman spectra of the $B_{1g}^{(1)}$, $B_{1g}^{(2)}$, and $B_{1g}^{(6)}$ phonon peaks at representative temperatures (plotted without Bose correction). Vertical dashed lines mark the phonon energy at 160 K. (h) Atomic displacements for the octahedral breathing mode (arrows), which are inverted under a 90° rotation (indicated by the blue star) representing the B_{1g} symmetry.

is not a simple consequence of spin-phonon coupling, but signals the presence of a underlying lattice softening driven by a separate degree of freedom.

We interpret this pronounced lattice softening as the experimental signature of an incipient lattice instability. Recent theoretical calculations predict that the spin disproportionation in $\text{La}_3\text{Ni}_2\text{O}_7$ can drive a static checkerboard-type lattice distortion (space group $Pmnm$), characterized by an imaginary mode frequency of the unstable oxygen breathing phonon [48]. This in-plane oxygen breathing mode corresponds specifically to the B_{1g} representation [Fig. 4(h)]. Consequently, the dramatic softening observed in the $B_{1g}^{(1)}$ mode suggests that the dynamic tendency toward the Ni-O bond disproportionation, manifesting as oxygen breathing modulations, persists in $\text{La}_3\text{Ni}_2\text{O}_7$ from 280 down to 4.5 K. In contrast to the theoretical prediction, however, our experimental results show that the soft $B_{1g}^{(1)}$ mode remains at a finite frequency, suggesting that the Ni-O bond disproportionation should remain dynamic without freezing into a static checkerboard structure. This interpretation is consistent with the reported persistence of the *Amam* phase at ambient pressure rather than a transition to the lower-symmetry *Pmnm* phase [48].

Furthermore, this dynamic Ni-O bond disproportionation provides a natural microscopic mechanism for the site-selective magnetic state. By favoring inequivalent, long and short Ni-O bond environments, it modulates the ligand-hole hybridization, thereby resulting in the two different nickel spin moments confirmed by our 2M data. Our work thus offers evidence for a latent, dynamic lattice instability that persists even in the low-temperature regime where the site-selective magnetic order is stabilized. The intrinsic tendency towards the bond disproportionation indicates that the complete description of the nickelate superconductors cannot be based on the magnetism alone, but must explicitly account for the coupling between this proximate electronic instability and the magnetic order as a fundamental ingredient.

VI. CONCLUSIONS

In this work, we investigate the evolution of the coupled electronic, magnetic, and phononic excitations in $\text{La}_3\text{Ni}_2\text{O}_7$ crystals. Based on symmetry-resolved analysis and model calculations, we establish the presence of two competing, direct spin exchange interactions (J_{2a} and J_{2b}) along the diagonal directions, identifying a key distinction between these layered nickelates and the cuprates. In the bilayer nickelates, three in-plane exchange interactions *inherently* compete one another, leading to diagonal spin stripe propagation in the low-pressure orthorhombic phase and likely driving magnetic frustration in the superconducting tetragonal phase. Our findings demonstrate that, while nickel $d_{3z^2-r^2}$ orbitals enforce the AF bilayer dimerization, the intralayer magnetism is governed by an intricate competition between the in-plane spin interactions mediated by the $d_{x^2-y^2}$ orbitals.

Furthermore, we identify low-energy magnetic modes corresponding to collective excitations of the small nickel moment (m_2), providing strong evidence of spin disproportionation in $\text{La}_3\text{Ni}_2\text{O}_7$. We also find an intriguing anomaly in the phononic sector: an anomalous softening of the B_{1g} phonons that persists from room temperature down to 4.5 K. As the breathing B_{1g} mode drives the checkerboard-type lattice modulations, we propose that an incipient bond or charge disproportionation serves as the common underlying driver for both the site-selective spin moments and the incipient lattice instability. This reveals that the SDW ground state is inextricably coupled to lattice

softness a central feature governing the intertwined spin and charge density dynamics in $\text{La}_3\text{Ni}_2\text{O}_7$.

ACKNOWLEDGEMENTS

D.H.G. and K.H.K. appreciate Beom Hyun Kim for helpful discussions. This work is supported by the Ministry of Education (No. 2021R1A6C101B418) and by the National Research Foundation of Korea grant funded by the Ministry of Science and ICT (No. RS 2024-00338707, No. RS-2023-00220471, and No. 2022M3K2A1083855). M.W. was supported by the National Natural Science Foundation of China (Grant No. 12425404) and the Guangdong Major Project of Basic Research (2025B0303000004).

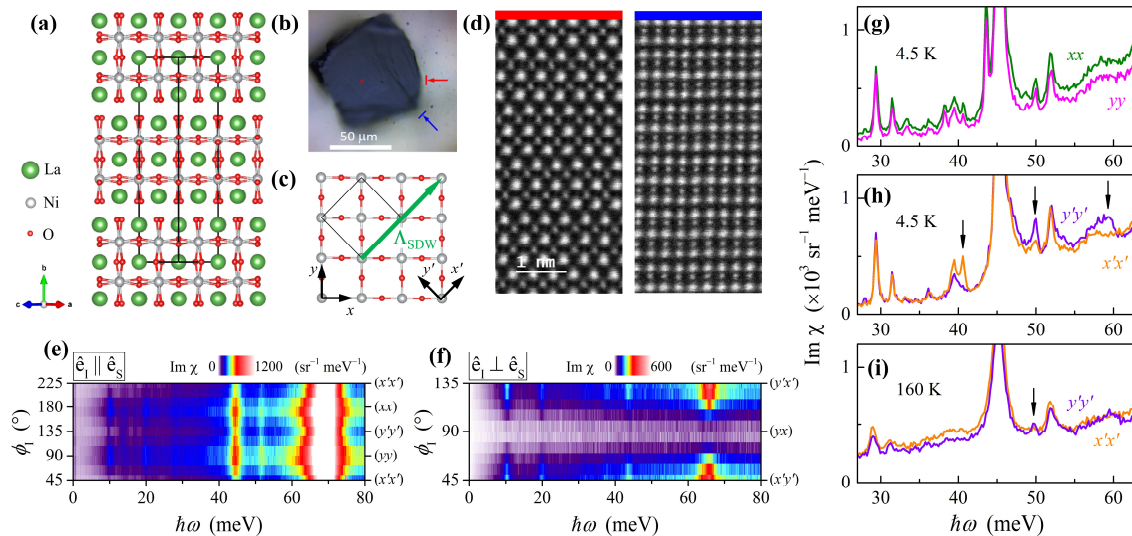


FIG. 5. Crystal structure and angular dependence. (a) Crystal structure of $\text{La}_3\text{Ni}_2\text{O}_7$. (b) Optical image of a $\text{La}_3\text{Ni}_2\text{O}_7$ crystal. (c) Schematic of a single NiO_2 plane, defining the tetragonal (x, y) and rotated (x', y') axes for Raman measurements, and the orientation of the SDW ordering vector, Λ_{SDW} (green arrow). The orthorhombic unit cell is indicated by the black solid lines in (a) and (c). (d) HAADF STEM images of $\text{La}_3\text{Ni}_2\text{O}_7$ crystal cross-sections viewed from the directions indicated by red and blue arrows in (b). (e), (f) Angular dependence of the room-temperature Raman response for parallel (e) and perpendicular (f) linear-polarization configurations as a function of the angle (ϕ_I) between the x -axis and the incident laser polarization. (g)-(i) Low-temperature spectra showing subtle evidence of the orthorhombic distortion. While spectra in the (xx) and (yy) geometries are nearly identical (g), a few phonon modes (indicated by arrows) exhibit different intensities in ($x'x'$) versus ($y'y'$) geometries [(h), (i)], confirming the inequivalence of the x' and y' axes.

APPENDIX A: EXPERIMENTAL METHODS

$\text{La}_3\text{Ni}_2\text{O}_7$ single crystals were synthesized in an optical floating-zone furnace under a high oxygen pressure of 15 bar. For Raman measurements, fresh crystal surfaces are obtained by mechanical cleavages. The crystal structure and crystallographic orientation were characterized by scanning transmission electron microscopy (STEM) using a Cs-corrected system (JEM-ARM200F, JEOL) at an acceleration voltage of 200 kV. Cross-sectional lamellae for STEM analysis were prepared using a focused ion beam (FIB) system (Helios Nanolab 650). Both FIB fabrication and STEM measurements were performed at the National Center for Inter-university Research Facilities (NCIRF) at Seoul National University. Representative optical and the high-angle annular dark-field (HAADF) STEM images are shown in Figure 5.

The temperature-dependent polarized Raman experiments were performed using a commercial micro-Raman system (XperRam200, NanoBase) equipped with a 532-nm laser. The laser power was kept below 0.1 mW to minimize sample heating. An objective lens with a numerical aperture of 0.6 was used to focus the linearly polarized laser to a spot size of $< 2 \mu\text{m}$ on the cleaved $\text{La}_3\text{Ni}_2\text{O}_7$ crystal surface and to collect the backscattered light. Incident and scattered light polarizations were controlled using half and quarter waveplates and analyzed with linear polarizers. Notch filters were used to reject elastically reflected light. Samples were mounted in a continuous liquid-He cryostat, cooled down to the base temperature of 4.5 K, and warmed up for the temperature-dependent measurements.

The Raman response, $\text{Im } \chi$, was determined from the charge-coupled device (CCD) photocounts by correcting for the Bose–Einstein factor $n_B(\hbar\omega, T) = (e^{\hbar\omega/k_B T} - 1)^{-1}$ and converting to the absolute unit ($\text{meV}^{-1} \text{sr}^{-1}$) using the relation:

$$\text{Im } \chi(\omega) = \frac{1}{1 + n_B(\hbar\omega, T)} \frac{\pi}{r_0^2} \frac{\omega_I}{\omega_S} \frac{d^2\sigma}{\hbar d\omega d\Omega}.$$

Here, $r_0 = e^2/(4\pi\epsilon_0 m_0 c^2)$ is the Thomson electron radius, $\omega_{I/S}$ is the incident/scattered light frequencies, and $\frac{d^2\sigma}{\hbar d\omega d\Omega}$ is the differential Raman scattering cross section calculated from the laser power, the acquisition time, the beam size, the energy shift intervals ($\hbar d\omega$) between CCD pixels, and the solid angle (Ω) of the collecting lens, with instrumental throughput assumed to be constant.

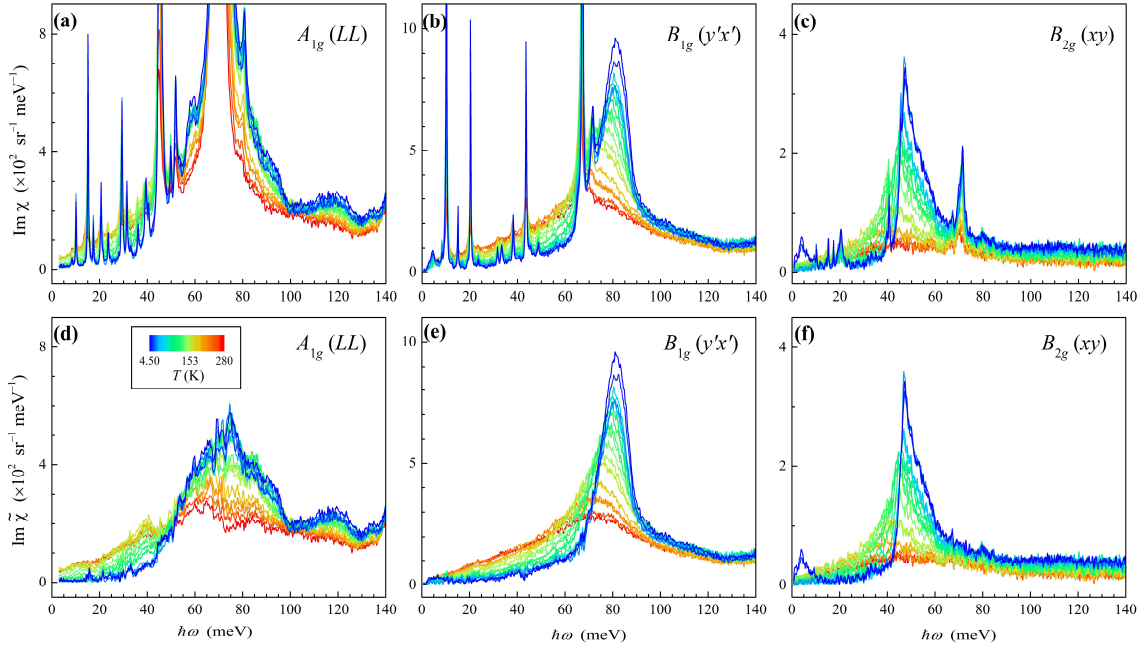


FIG. 6. $\text{La}_3\text{Ni}_2\text{O}_7$ Raman response before and after phonon subtraction. (a)-(c) The raw Raman response ($\text{Im } \chi$) for the A_{1g} , B_{1g} , and B_{2g} symmetry channels, respectively. Sharp phonon peaks are superimposed on the broader electronic and magnetic continua. (d)-(f) The phonon-subtracted Raman response ($\text{Im } \tilde{\chi}$) obtained after fitting the phonon peaks to Lorentzian functions and subtracting them from the raw response, which isolates the electronic and magnetic contributions discussed in the main text.

Complementary Raman measurements were performed using a macro-Raman system equipped with a triple-stage spectrometer (TriVista, Princeton Instruments) and a closed-cycle magneto-optical cryostat (SpectromagPT, Oxford Instruments). The Raman data in the out-of-plane magnetic fields $B = 0, 7$ T at the base temperature (2 K) were collected using a 514.5-nm laser source with a power of 5 mW and a spot diameter of about 50 μm in the circularly polarized (RL) configuration.

APPENDIX B: ANALYSIS AND SUBTRACTION OF PHONON PEAKS

To isolate the electronic and magnetic contributions, the phonon peaks were fitted to Lorentzian profiles and subtracted from the spectra, yielding the phonon-subtracted response, $\text{Im } \tilde{\chi}$. The raw and phonon-subtracted Raman responses are compared in Fig. 6. The temperature dependence of the phonon energies is summarized in Figs. 4(a)-(d) and Fig. 7.

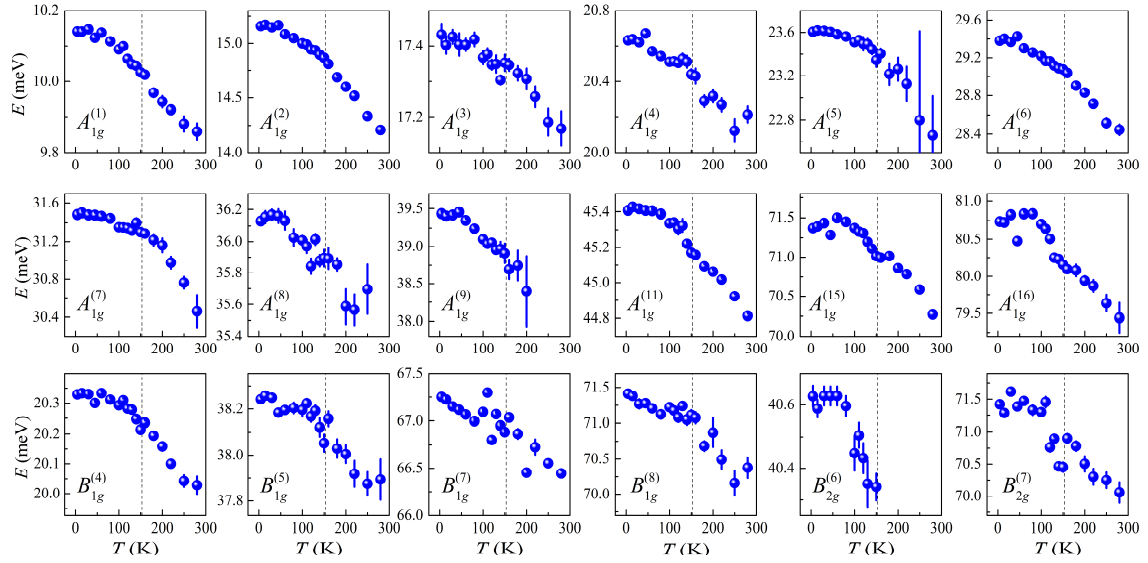


FIG. 7. Temperature dependence of the energies for representative optical phonons that exhibit typical anharmonic hardening upon cooling, as determined by the Lorentzian fitting analysis. This contrasts with the soft B_{1g} modes shown in Fig. 4 in the main text. The vertical dashed line indicates T_{SDW} .

APPENDIX C: TETRAGONAL APPROXIMATION

In the main text, we analyze our Raman data using the tetragonal D_{4h} point group. We note that the true crystallographic structure of $\text{La}_3\text{Ni}_2\text{O}_7$ at ambient pressure is orthorhombic ($Am\bar{a}m$, D_{2h}) due to slight lattice distortions. However, the experimental evidence demonstrates that the system behaves as effectively tetragonal, making the D_{4h} framework the appropriate and most physically relevant choice for interpreting the data.

TABLE II. Raman-active symmetry channels in each point group

$(\hat{\mathbf{e}}_I \hat{\mathbf{e}}_S)$	D_{4h}	D_{2h}
$(xx), (yy)$	$A_{1g} + B_{1g}$	$A_g + B_{1g}$
$(x'x'), (y'y')$	$A_{1g} + B_{2g}$	A_g
$(xy), (yx)$	$B_{2g} (+ A_{2g})$	A_g
$(x'y'), (y'x')$	$B_{1g} (+ A_{2g})$	B_{1g}
$(LL), (RR)$	$A_{1g} (+ A_{2g})$	A_g
$(LR), (RL)$	$B_{1g} + B_{2g}$	$A_g + B_{1g}$

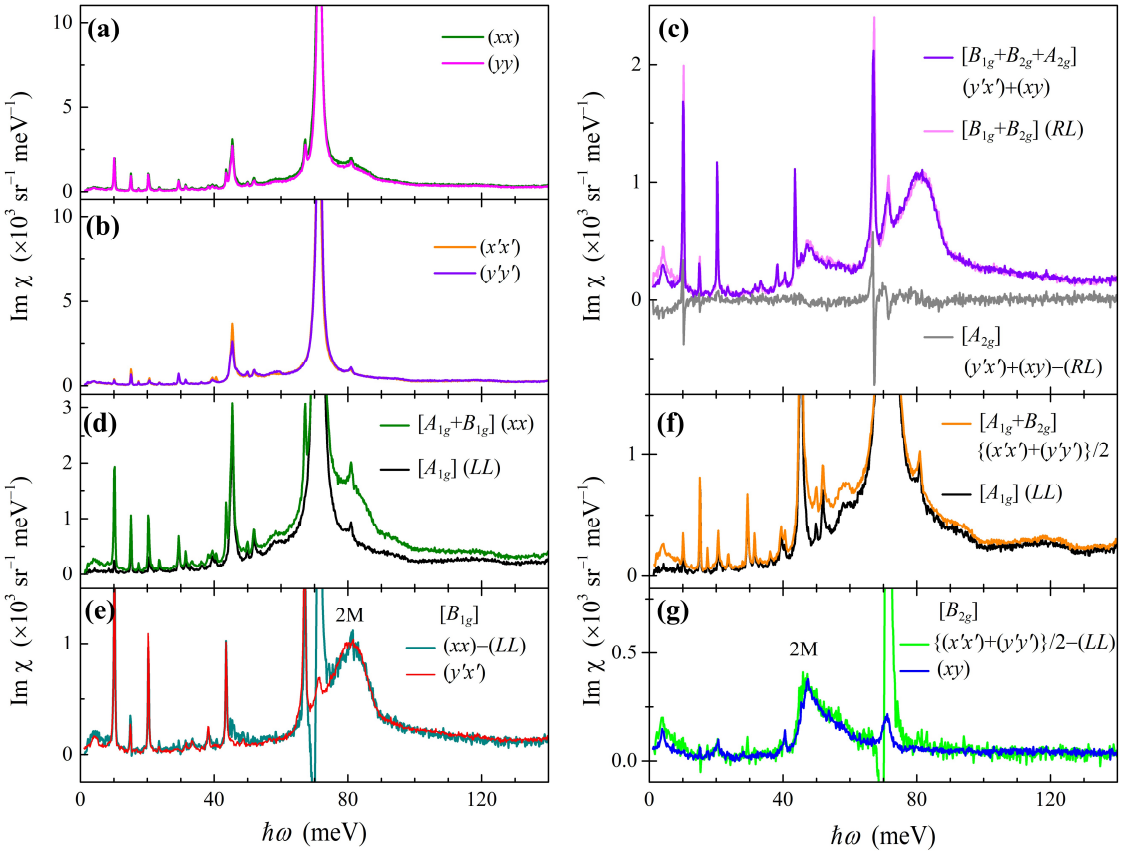


FIG. 8. Polarization-resolved analysis at 4.5 K. (a),(b) Comparison of the parallel-polarized spectra, between (xx) and (yy) geometries (a) and between (x'x') and (y'y') geometries (b). (c) Isolation of the A_{2g} signal from the combination of the (y'x'), (xy), and (RL) spectra. The resulting A_{2g} response (grey) is nearly zero for the entire energy range, except for the residuals from the subtraction of sharp phonon peaks. (d),(e) Validation of the B_{1g} channel assignment. The B_{1g} response is probed directly from the (y'x') spectrum [red in (e)] and can also be isolated by subtracting the pure A_{1g} (LL) component from the (xx) spectrum [black and olive in (d)]. Both methods yield nearly identical spectra for the 2M peak (e), confirming the B_{1g} assignment. (f),(g) Validation of the B_{2g} channel assignment. Similarly, the B_{2g} response is measured directly in the (xy) spectrum [blue in (g)] and isolated from the (x'x')+(y'y') spectrum [orange in (f)]. Comparison of the both methods (g) demonstrate that the corresponding 2M peak is consistent with the B_{2g} assignment.

Most importantly, the Raman responses in the (xy) and (LL) scattering geometries are completely different [Figs. 2(a),(c)]. Under the strict D_{2h} symmetry, both geometries would probe the same A_g representation (Table II), and their spectra would be expected to be similar or heavily intermixed. In contrast, under tetragonal D_{4h} symmetry, these geometries select distinct symmetry channels, B_{2g} and A_{1g} , respectively. The pronounced

experimental difference between these two channels therefore confirms that any symmetry-lowering effects from the orthorhombic distortion are negligible for the electronic and magnetic excitations central to this study.

The effective tetragonal symmetry is further corroborated by the angular dependence of the Raman intensity. At room temperature, the response exhibits a clear four-fold rotational symmetry, with intensity maxima and minima alternating every 45° [Figs. 5(e),(f)]. This is a definitive signature of underlying tetragonal electronic and lattice properties, a behavior also reported in the trilayer nickelate $\text{La}_4\text{Ni}_3\text{O}_{10}$ [42]. While the tetragonal response is dominant, we do observe subtle evidence of the orthorhombic structure in a few low-temperature phonon modes, characterized by different intensities in the $(x'x')$ and $(y'y')$ polarizations [Figs. 5(g)-(i)] as x' and y' are two inequivalent orthorhombic axes. Despite these minor modulations of the phonon intensities, the overall Raman response including the two-magnon (2M) features in the B_{1g} and B_{2g} channels has nearly four-fold rotational dependence at low temperatures [Figs. 8(a),(b)]. This confirms that the tetragonal approximation is robust and provides the insightful basis for the central discoveries in our work: electronic gap, 2M peaks, and soft B_{1g} phonons.

Finally, we also investigated the possibility of an A_{2g} signal, which would indicate a chiral or time-reversal symmetry-broken state. The A_{2g} response can be isolated by subtracting a (RL) spectrum from the sum of (xy) and $(y'x')$ spectra. However, this analysis yielded no discernible evidence for the A_{2g} signal [Fig. 8(c)]. Accordingly, the A_{2g} channel is not considered in our main analysis.

APPENDIX D: ASSIGNMENT OF THE 2M RESPONSE

1. *Exclusion of alternative origins for the B_{1g} and B_{2g} peaks*

In this section, we systematically describe the reasonings to rule out alternative interpretations for the prominent peaks observed in the B_{1g} and B_{2g} $\text{Im } \tilde{\chi}$ spectra.

First, phononic origins can be firmly excluded. A two-phonon scattering process is inconsistent with our data because of symmetry selection rules. The product of two identical irreducible representations (e.g., $B_{1g} \otimes B_{1g}$ or $B_{2g} \otimes B_{2g}$) always contains the fully

symmetric A_{1g} representation, resulting in any two-phonon signal strongest in the A_{1g} channel. Since the low- and high-energy peaks of the B_{1g} and B_{2g} channels are not observed in our A_{1g} (LL) spectra, a two-phonon assignment is untenable. Furthermore, the possibility of a Kohn anomaly related to a CDW instability is also ruled out, as such an anomaly would cause phonon softening. In contrast, the high-energy B_{1g} and B_{2g} peaks exhibit hardening below T_{SDW} .

Second, the peaks cannot be attributed to single magnon excitations due to clear violations of selection rules and energy considerations. Single magnon scattering is forbidden in parallel linear polarization geometries [30]. However, the B_{1g} and B_{2g} peaks are clearly observed in such configurations [Figs. 4(d)-(g)]. Moreover, the observed peak energies (47 and 81 meV) are inconsistent with the reported single-magnon energy (~ 70 meV) at the Γ -point [24].

Finally, an electronic origin, such as an interband transition across the SDW gap, is inconsistent with the temperature dependence of the spectral weight (SW). The opening of the SDW gap abruptly depletes low-energy SW [Figs. 2(a),(d)], which would be transferred to higher energies. This requires that the SW of any interband transition related to the SDW gap should increase more steeply below T_{SDW} to compensate for the gapping. However, the SW evolution of the high-energy B_{1g} and B_{2g} peaks actually *decreases* below T_{SDW} [red squares in Figs. 9(b),(c)], in direct opposition to this expectation. The low-energy features below 15 meV are also unlikely to have an electronic origin, because their energy is far below the main SDW gap scale, marked by the isosbestic point near 50 meV. Furthermore, their sharp emergence only below 30 K is incompatible with a Drude response from free carriers, which would be gapped out at the much higher $T_{SDW} = 153$ K.

2. Analysis of the detailed temperature dependence

In contrast to the scenarios discussed above, the two-magnon (2M) interpretation is fully consistent with our experiments, demonstrated by the excellent agreement between our data and theoretical calculations in the main text. Furthermore, the detailed temperature evolution of the peaks in the B_{1g} and B_{2g} channels exhibits the characteristic hallmarks of 2M scattering observed in numerous other antiferromagnets, as we delineate below.

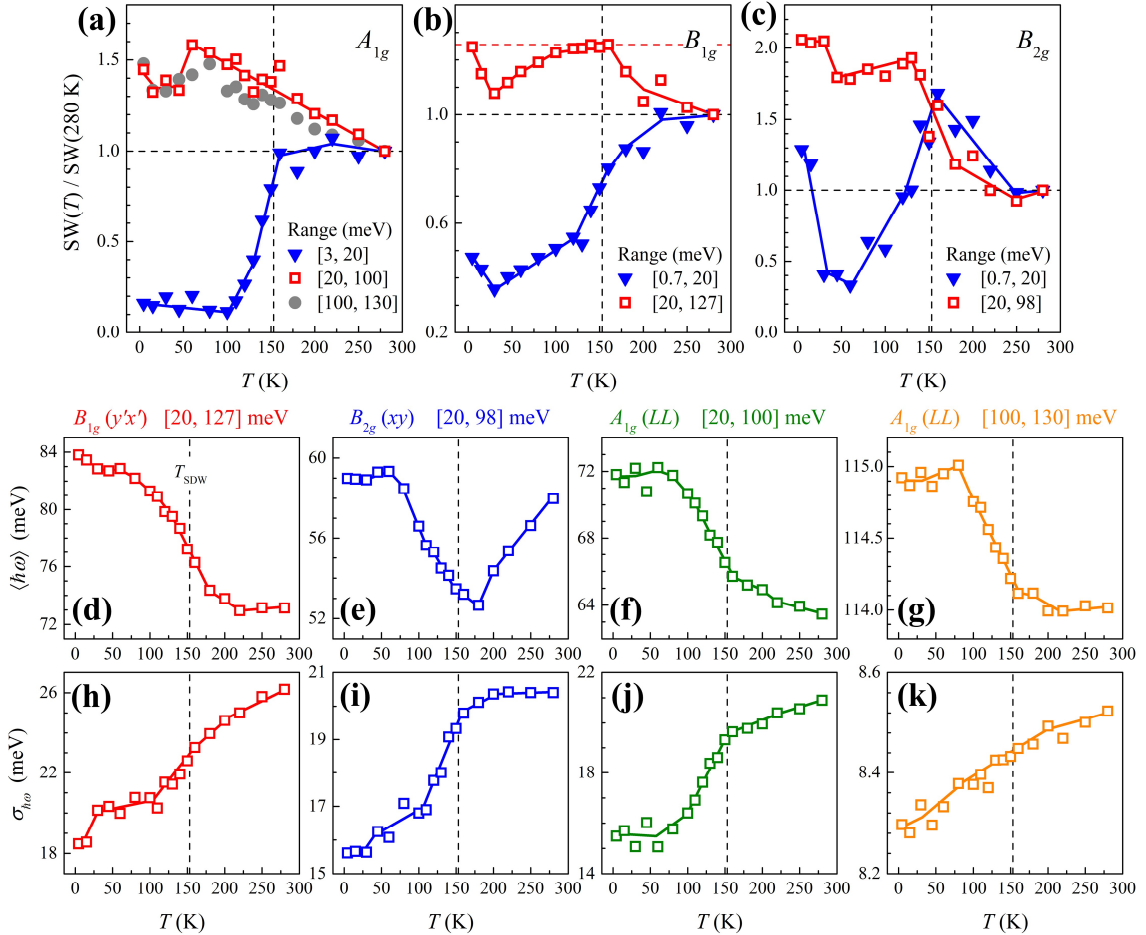


FIG. 9. Temperature dependence of the 2M peak characteristics. (a)-(c) SW evolution for each symmetry channel integrated over the low (blue) and high (red, grey) energy ranges, normalized by the values at 280 K. (d)-(g) Mean energies and (h)-(k) standard deviations (spectral widths) of the 2M spectral features as functions of temperature, calculated over the energy ranges indicated above each panel. The vertical dashed line marks T_{SDW} . Solid lines are guide for the eye.

First, the lineshape evolution follows the expected behaviors of the 2M peaks. Above the magnetic ordering temperature, 2M scattering arises from short-range spin fluctuations (paramagnons), typically resulting in broad spectral features. Below the transition, the establishment of long-range order leads to well-defined magnons, causing the 2M peak to both sharpen and harden. This is precisely what we observe in $\text{La}_3\text{Ni}_2\text{O}_7$: Upon cooling below T_{SDW} , the mean energy of the B_{1g} and B_{2g} peaks increases while their spectral width decreases [Figs. 9(d)-(k)].

Second, the temperature dependence of the integrated SW provides quantitative confirmation. Above T_{SDW} , the 2M SW depends on the local spin quantum number S ,

decreasing upon cooling for $S \geq 1$ systems but increasing for low-spin $S < 1$ systems [33]. In $\text{La}_3\text{Ni}_2\text{O}_7$, the SW increases upon cooling above T_{SDW} before peaking near the transition [red squares in Figs. 9(b),(c)], indicating low-spin $S < 1$ states which is consistent with the previous estimates of nickel spin moments lower than $1 \mu_{\text{B}}$ [3,26,28]. The subsequent suppression of the SW below T_{SDW} is a consequence of the reduced dynamic spin-spin correlations upon the onset of the magnetic order [33], a behavior also seen in other antiferromagnets [34,35].

3. Excitation wavelength and magnetic field dependence

To further validate our assignment and rule out potential artifacts, we performed complementary measurements using a 514.5-nm laser in a circular (RL) polarization geometry, which simultaneously probes the B_{1g} and B_{2g} responses, under out-of-plane magnetic fields of $B = 0$ and 7 T. As shown in Fig. 10, the prominent 2M features observed with the 532-nm laser are clearly reproduced in the 514.5-nm data. The persistence of these peaks at a different excitation wavelength provides definitive evidence that they are intrinsic Raman scattering signals and not fluorescent artifacts.

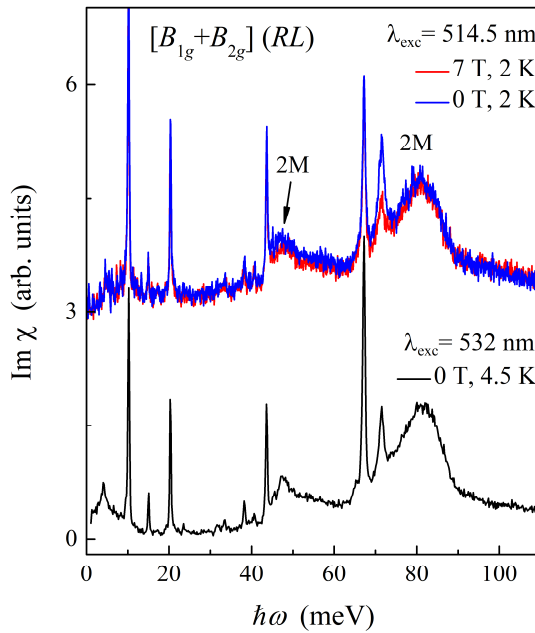


FIG. 10. Comparison of the low-temperature (RL) Raman response measured with two different laser excitation wavelengths (532 and 514.5 nm) and at out-of-plane magnetic fields of $B = 0$ and 7 T. The key spectral features are robust against changes in both wavelength and magnetic field, confirming their origin as 2M Raman scattering.

Furthermore, a comparison of the 0 and 7 T data reveals that the 2M features are robust against the applied magnetic field, which is a well-known characteristic of 2M Raman scattering [30]. The primary reason is that the 2M process in the Raman scattering involves two opposite spin-flips, whose individual Zeeman energy shifts cancel each other out, leading to no net energy shift. In addition, even in the case of a complete spin-flop phase, the Zeeman energy itself (~ 0.4 meV at 7 T) is orders of magnitude smaller than the widths (> 20 meV) of the broad 2M peaks, making any potential shift negligible and hardly observable.

4. Discussion of the high-energy A_{1g} features

Lastly, we address the origin of the broad, high-energy humps observed in the A_{1g} channel. Their smooth SW evolution across T_{SDW} increasing upon cooling [red and grey in Fig. 9(a)] might suggest a non-magnetic origin, such as interband electron transitions or multiphonon scattering. However, we find that these features can also be explained by a 2M origin, which become allowed in bilayer systems. Specifically, in a bilayer antiferromagnet, a 2M signal in the A_{1g} channel can be generated when the interlayer exchange interaction J_c is present, as it breaks the commutation relation between the Heisenberg Hamiltonian ($\mathcal{H}_{\text{2LAF}}$) and the A_{1g} (LL) Fleury-Loudon scattering operator (\mathcal{H}_{FL}) [49]. Indeed, the temperature dependence of the mean energies and spectral widths of the A_{1g} response resembles that of the B_{1g} and B_{2g} 2M peaks [Figs. 9(d)-(k)].

While the precise form of the magnon-magnon interaction vertex (J_α) for the A_{1g} (LL) scattering channel is not obviously known, we performed the model calculation (Fig. 11) using a phenomenological assumption of $J_\alpha = 2J_3$. Consequently, the calculation reproduces the key aspects of the high-energy A_{1g} response, including its spectral distribution and relative intensity [Fig. 11(b)]. This interpretation is further supported by observations in the bilayer iridate $\text{Sr}_3\text{Ir}_2\text{O}_7$, where A_{1g} 2M peaks with a similar temperature dependence have also been reported [39]. We note that a simpler assumption of $J_\alpha = J_c$ fails in this case, as the large value of J_c completely suppresses the renormalized response. While our results may indicate a 2M origin of the A_{1g} features, future theoretical works with a more rigorous treatment on the higher-order effects are required for the complete understanding of the high-energy A_{1g} response.

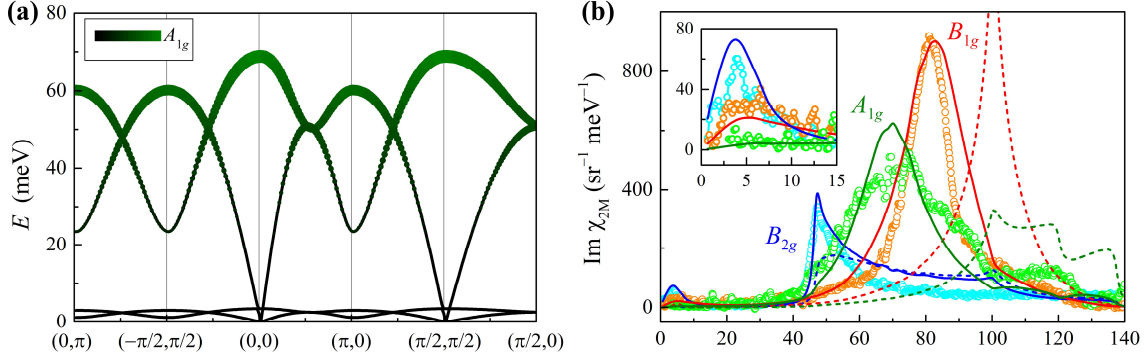


FIG. 11. Calculation of the 2M peak in the A_{1g} channel. (a) The A_{1g} scattering matrix element strength superimposed on the calculated magnon dispersion. (b) Calculated bare (dashed) and interacting (solid lines) 2M responses in the three symmetry channels. To obtain the A_{1g} response, a phenomenological magnon-magnon interaction vertex of $J_\alpha = 2J_3$ was assumed. The A_{1g} , B_{1g} , and B_{2g} data at 4.5 K (green, orange, cyan circles) are compared with the theoretical spectra. High-energy quadratic backgrounds are removed from the A_{1g} and B_{1g} data.

APPENDIX E: THEORETICAL CALCULATION OF THE 2M RESPONSE

The magnon dispersion was calculated starting from the bilayer antiferromagnetic (2LAF) Heisenberg Hamiltonian

$$\mathcal{H}_{2\text{LAF}} = \sum_{\langle i,j \rangle} J_{ij} \mathbf{S}_i \cdot \mathbf{S}_j = \sum_{\langle i,j \rangle} J_{ij} \left[S_i^z S_j^z + \frac{S_i^+ S_j^- + S_i^- S_j^+}{2} \right] \quad (3)$$

where S_i^z is the component along the easy axis $\perp \mathbf{Q}_{\text{SDW}}$ and $S_i^\pm = S_i^x \pm iS_i^y$. The model incorporates the eight distinct magnetic sublattices $\{a, b, \dots, h\}$, with the top $\{a, b, c, d\}$ and bottom $\{e, f, g, h\}$ layers coupled antiferromagnetically: $S_1 = S_a = -S_c = -S_e = S_g = m_1/g\mu_B$ and $S_2 = S_b = -S_d = -S_f = S_h = m_2/g\mu_B$ (Fig. 12).

The Hamiltonian was linearized using the leading-order Holstein–Primakoff transformations,

$$\begin{aligned} j \in a: \quad & S_j^+ \simeq \sqrt{2S_1}a_j, \quad S_j^- \simeq \sqrt{2S_1}a_j^\dagger, \quad S_j^z = S_1 - a_j^\dagger a_j; \\ j \in b: \quad & S_j^+ \simeq \sqrt{2S_2}b_j, \quad S_j^- \simeq \sqrt{2S_2}b_j^\dagger, \quad S_j^z = S_2 - b_j^\dagger b_j; \\ j \in c: \quad & S_j^+ \simeq \sqrt{2S_1}c_j^\dagger, \quad S_j^- \simeq \sqrt{2S_1}c_j, \quad S_j^z = -S_1 - c_j c_j^\dagger; \\ j \in d: \quad & S_j^+ \simeq \sqrt{2S_2}d_j^\dagger, \quad S_j^- \simeq \sqrt{2S_2}d_j, \quad S_j^z = -S_2 - d_j d_j^\dagger; \\ & \vdots \\ j \in h: \quad & S_j^+ \simeq \sqrt{2S_2}h_j, \quad S_j^- \simeq \sqrt{2S_2}h_j^\dagger, \quad S_j^z = S_2 - h_j^\dagger h_j. \end{aligned}$$

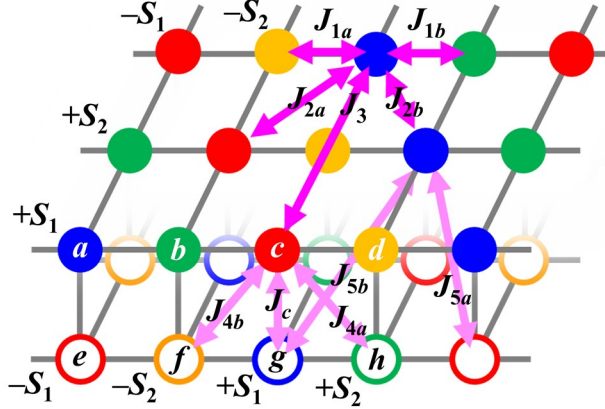


FIG. 12. Schematic of the magnetic sublattice structure used in the theoretical model, defining the eight distinct nickel sublattices $\{a, b, \dots, h\}$. The structure consists of high-moment ($\pm S_1$, blue and red) and low-moment ($\pm S_2$, green and orange) sites. The figure illustrates the intralayer ($J_{1a,b}, J_{2a,b}, J_3$) and interlayer ($J_{4a,b}, J_{5a,b}, J_c$) exchange interactions included in the Heisenberg Hamiltonian. The subscripts ‘a’ and ‘b’ distinguish interactions ($J_{1a,b}, J_{2a,b}, J_{4a,b}, J_{5a,b}$) between sites with antiparallel (a) and parallel (b) spin alignments, respectively. The interactions not included in Table I ($J_{1a,b}, J_{4a,b}, J_{5a,b}$) are set to zero in the numerical calculation of Fig. 3.

Applying the Fourier transform (e.g., $a_j = \frac{1}{\sqrt{N}} \sum_{\mathbf{k}} e^{-i\mathbf{k} \cdot \mathbf{r}_j} a_{\mathbf{k}}$ and $a_j^\dagger = \frac{1}{\sqrt{N}} \sum_{\mathbf{k}} e^{i\mathbf{k} \cdot \mathbf{r}_j} a_{\mathbf{k}}^\dagger$), the Hamiltonian in Eq. (3) can be written in matrix form $\mathcal{H}_{\text{2LAF}} = \sum_{\mathbf{k}} \Phi_{\mathbf{k}}^\dagger K_{\mathbf{k}} \Phi_{\mathbf{k}}$, where $\Phi_{\mathbf{k}} = (a_{\mathbf{k}}, b_{\mathbf{k}}, c_{\mathbf{k}}^\dagger, d_{\mathbf{k}}^\dagger, e_{\mathbf{k}}^\dagger, f_{\mathbf{k}}^\dagger, g_{\mathbf{k}}, h_{\mathbf{k}})^T$ is the vector of bosonic operators. The matrix elements of the dynamical matrix

$$K_{\mathbf{k}} = \begin{pmatrix} K_{\mathbf{k}}^{(aa)} & K_{\mathbf{k}}^{(ab)} & K_{\mathbf{k}}^{(ac)} & K_{\mathbf{k}}^{(ad)} & K_{\mathbf{k}}^{(ae)} & K_{\mathbf{k}}^{(af)} & K_{\mathbf{k}}^{(ag)} & K_{\mathbf{k}}^{(ah)} \\ K_{-\mathbf{k}}^{(ab)} & K_{\mathbf{k}}^{(bb)} & K_{-\mathbf{k}}^{(ad)} & K_{\mathbf{k}}^{(bd)} & K_{-\mathbf{k}}^{(af)} & K_{\mathbf{k}}^{(bf)} & K_{-\mathbf{k}}^{(ah)} & K_{\mathbf{k}}^{(bh)} \\ K_{\mathbf{k}}^{(ac)} & K_{\mathbf{k}}^{(ad)} & K_{\mathbf{k}}^{(aa)} & K_{\mathbf{k}}^{(ab)} & K_{\mathbf{k}}^{(ag)} & K_{\mathbf{k}}^{(ah)} & K_{\mathbf{k}}^{(ae)} & K_{\mathbf{k}}^{(af)} \\ K_{-\mathbf{k}}^{(ad)} & K_{\mathbf{k}}^{(bd)} & K_{-\mathbf{k}}^{(ab)} & K_{\mathbf{k}}^{(bb)} & K_{-\mathbf{k}}^{(ah)} & K_{\mathbf{k}}^{(bh)} & K_{-\mathbf{k}}^{(af)} & K_{\mathbf{k}}^{(bf)} \\ K_{\mathbf{k}}^{(ae)} & K_{\mathbf{k}}^{(af)} & K_{\mathbf{k}}^{(ag)} & K_{\mathbf{k}}^{(ah)} & K_{\mathbf{k}}^{(aa)} & K_{\mathbf{k}}^{(ab)} & K_{\mathbf{k}}^{(ac)} & K_{\mathbf{k}}^{(ad)} \\ K_{-\mathbf{k}}^{(af)} & K_{\mathbf{k}}^{(bf)} & K_{-\mathbf{k}}^{(ah)} & K_{\mathbf{k}}^{(bh)} & K_{-\mathbf{k}}^{(ab)} & K_{\mathbf{k}}^{(bb)} & K_{-\mathbf{k}}^{(ad)} & K_{\mathbf{k}}^{(bd)} \\ K_{\mathbf{k}}^{(ag)} & K_{\mathbf{k}}^{(ah)} & K_{\mathbf{k}}^{(ae)} & K_{\mathbf{k}}^{(af)} & K_{\mathbf{k}}^{(ac)} & K_{\mathbf{k}}^{(ad)} & K_{\mathbf{k}}^{(aa)} & K_{\mathbf{k}}^{(ab)} \\ K_{-\mathbf{k}}^{(ah)} & K_{\mathbf{k}}^{(bh)} & K_{-\mathbf{k}}^{(af)} & K_{\mathbf{k}}^{(bf)} & K_{-\mathbf{k}}^{(ad)} & K_{\mathbf{k}}^{(bd)} & K_{-\mathbf{k}}^{(ab)} & K_{\mathbf{k}}^{(bb)} \end{pmatrix} \quad (4)$$

for each momentum vector \mathbf{k} are functions of J_{ij} , S_1 , and S_2 :

$$K_{\mathbf{k}}^{(aa)} = 2J_{2b}S_1 \cos(k_x - k_y) + 2S_1(J_{2a} - J_{2b} + 2J_3 + J_{5a} - J_{5b}) + J_c S_1 + 2S_2(J_{1a} - J_{1b} + J_{4a} - J_{4b}),$$

$$\begin{aligned}
K_{\mathbf{k}}^{(bb)} &= 2J_{2b}S_2 \cos(k_x - k_y) + 2S_2(J_{2a} - J_{2b} + 2J_3 + J_{5a} - J_{5b}) + J_cS_2 \\
&\quad + 2S_1(J_{1a} - J_{1b} + J_{4a} - J_{4b}), \\
K_{\mathbf{k}}^{(ab)} &= J_{1b}\sqrt{S_1S_2}(e^{-ik_x} + e^{-ik_y}), \quad K_{\mathbf{k}}^{(ad)} = J_{1a}\sqrt{S_1S_2}(e^{ik_x} + e^{ik_y}), \\
K_{\mathbf{k}}^{(ac)} &= 2S_1(J_{2a} \cos(k_x + k_y) + J_3(\cos 2k_x + \cos 2k_y)), \\
K_{\mathbf{k}}^{(bd)} &= 2S_2(J_{2a} \cos(k_x + k_y) + J_3(\cos 2k_x + \cos 2k_y)), \\
K_{\mathbf{k}}^{(ae)} &= S_1(2J_{5a} \cos(k_x - k_y) + J_c), \quad K_{\mathbf{k}}^{(bf)} = S_2(2J_{5a} \cos(k_x - k_y) + J_c), \\
K_{\mathbf{k}}^{(af)} &= J_{4a}\sqrt{S_1S_2}(e^{-ik_x} + e^{-ik_y}), \quad K_{\mathbf{k}}^{(ah)} = J_{4b}\sqrt{S_1S_2}(e^{ik_x} + e^{ik_y}), \\
K_{\mathbf{k}}^{(ag)} &= 2J_{5b}S_1 \cos(k_x + k_y), \quad K_{\mathbf{k}}^{(bh)} = 2J_{5b}S_2 \cos(k_x + k_y).
\end{aligned}$$

The Hamiltonian $\mathcal{H}_{2\text{LAF}}$ was diagonalized by a generalized Bogoliubov transformation, which was obtained by solving the eigenvalue problem for the Bogoliubov-de Gennes (BdG) Hamiltonian, $(I_{\text{BdG}}K_{\mathbf{k}})\nu_i = \lambda_i\nu_i$, where $I_{\text{BdG}} = \text{diag}(1, 1, -1, -1, -1, -1, 1, 1)$ is the BdG metric. The resulting eigenvalues $\{\lambda_i\}$ give the magnon eigenenergies, $E_i(\mathbf{k}) = |\lambda_i|$, and the eigenvectors $\{\nu_i\}$ construct the corresponding Bogoliubov matrix $T_{\mathbf{k}} = (w_1, \dots, w_8)$ with $w_i = \sqrt{\frac{\text{sgn}(\lambda_i)}{\nu_i^\dagger I_{\text{BdG}} \nu_i}} \nu_i$. Such a Bogoliubov transformation $T_{\mathbf{k}}$ maps the original bosonic operators to the magnon eigenstates: $\Phi_{\mathbf{k}} = T_{\mathbf{k}}\Phi'_{\mathbf{k}}$, where $\Phi'_{\mathbf{k}} = (\alpha_{1,\mathbf{k}}, \alpha_{2,\mathbf{k}}, \alpha_{3,\mathbf{k}}, \alpha_{4,\mathbf{k}}, \alpha_{5,-\mathbf{k}}^\dagger, \alpha_{6,-\mathbf{k}}^\dagger, \alpha_{7,-\mathbf{k}}^\dagger, \alpha_{8,-\mathbf{k}}^\dagger)^T$ is the vector of magnon annihilation and creation operators. The Hamiltonian is diagonalized in the magnon eigenbasis $\Phi'_{\mathbf{k}}$:

$$\mathcal{H}_{2\text{LAF}} = \sum_{\mathbf{k}} \Phi_{\mathbf{k}}^\dagger K_{\mathbf{k}} \Phi_{\mathbf{k}} = \sum_{\mathbf{k}} \Phi'_{\mathbf{k}}^\dagger K'_{\mathbf{k}} \Phi'_{\mathbf{k}} = \sum_{\mathbf{k}} \sum_{i=1}^8 E_i(\mathbf{k}) \alpha_{i,\mathbf{k}}^\dagger \alpha_{i,\mathbf{k}}$$

where $K'_{\mathbf{k}} = T_{\mathbf{k}}^\dagger K_{\mathbf{k}} T_{\mathbf{k}}$ is the diagonal matrix of magnon eigenenergies.

After applying the same Holstein–Primakoff and Fourier transformations used for Eq. (3), the FL scattering Hamiltonian, Eq. (1), can also be written in a quadratic bosonic form $\mathcal{H}_{\text{FL}} = \sum_{\mathbf{k}} \Phi_{\mathbf{k}}^\dagger M_{\mathbf{k}} \Phi_{\mathbf{k}}$, where the scattering vertex matrix $M_{\mathbf{k}}$ depends on the Raman scattering channel. For the $B_{1g}(y'x')$ channel,

$$M_{\mathbf{k}} = \begin{pmatrix} 0 & M_{\mathbf{k}}^{(ab)} & M_{\mathbf{k}}^{(ac)} & M_{\mathbf{k}}^{(ad)} & 0 & M_{\mathbf{k}}^{(af)} & 0 & M_{\mathbf{k}}^{(ah)} \\ M_{-\mathbf{k}}^{(ab)} & 0 & M_{-\mathbf{k}}^{(ad)} & M_{\mathbf{k}}^{(bd)} & M_{-\mathbf{k}}^{(af)} & 0 & M_{-\mathbf{k}}^{(ah)} & 0 \\ M_{\mathbf{k}}^{(ac)} & M_{\mathbf{k}}^{(ad)} & 0 & M_{\mathbf{k}}^{(ab)} & 0 & M_{\mathbf{k}}^{(ah)} & 0 & M_{\mathbf{k}}^{(af)} \\ M_{-\mathbf{k}}^{(ad)} & M_{\mathbf{k}}^{(bd)} & M_{-\mathbf{k}}^{(ab)} & 0 & M_{-\mathbf{k}}^{(ah)} & 0 & M_{-\mathbf{k}}^{(af)} & 0 \\ 0 & M_{\mathbf{k}}^{(af)} & 0 & M_{\mathbf{k}}^{(ah)} & 0 & M_{\mathbf{k}}^{(ab)} & M_{\mathbf{k}}^{(ac)} & M_{\mathbf{k}}^{(ad)} \\ M_{-\mathbf{k}}^{(af)} & 0 & M_{-\mathbf{k}}^{(ah)} & 0 & M_{-\mathbf{k}}^{(ab)} & 0 & M_{-\mathbf{k}}^{(ad)} & M_{\mathbf{k}}^{(bd)} \\ 0 & M_{\mathbf{k}}^{(ah)} & 0 & M_{\mathbf{k}}^{(af)} & M_{\mathbf{k}}^{(ac)} & M_{\mathbf{k}}^{(ad)} & 0 & M_{\mathbf{k}}^{(ab)} \\ M_{-\mathbf{k}}^{(ah)} & 0 & M_{-\mathbf{k}}^{(af)} & 0 & M_{-\mathbf{k}}^{(ad)} & M_{\mathbf{k}}^{(bd)} & M_{-\mathbf{k}}^{(ab)} & 0 \end{pmatrix}, \quad (5)$$

$$\begin{aligned} M_{\mathbf{k}}^{(ab)} &= J_{1b}\sqrt{S_1S_2}(e^{-ik_x} - e^{-ik_y}), & M_{\mathbf{k}}^{(ad)} &= J_{1a}\sqrt{S_1S_2}(e^{ik_x} - e^{ik_y}), \\ M_{\mathbf{k}}^{(ac)} &= 2J_3S_1(\cos 2k_x - \cos 2k_y), & M_{\mathbf{k}}^{(bd)} &= 2J_3S_2(\cos 2k_x - \cos 2k_y), \\ M_{\mathbf{k}}^{(af)} &= J_{4a}\sqrt{S_1S_2}(e^{-ik_x} - e^{-ik_y}), & M_{\mathbf{k}}^{(ah)} &= J_{4b}\sqrt{S_1S_2}(e^{ik_x} - e^{ik_y}). \end{aligned}$$

For the B_{2g} (xy) channel,

$$M_{\mathbf{k}} = \begin{pmatrix} M_{\mathbf{k}}^{(aa)} & 0 & M_{\mathbf{k}}^{(ac)} & 0 & M_{\mathbf{k}}^{(ae)} & 0 & M_{\mathbf{k}}^{(ag)} & 0 \\ 0 & M_{\mathbf{k}}^{(bb)} & 0 & M_{\mathbf{k}}^{(bd)} & 0 & M_{\mathbf{k}}^{(bf)} & 0 & M_{\mathbf{k}}^{(bh)} \\ M_{\mathbf{k}}^{(ac)} & 0 & M_{\mathbf{k}}^{(aa)} & 0 & M_{\mathbf{k}}^{(ag)} & 0 & M_{\mathbf{k}}^{(ae)} & 0 \\ 0 & M_{\mathbf{k}}^{(bd)} & 0 & M_{\mathbf{k}}^{(bb)} & 0 & M_{\mathbf{k}}^{(bh)} & 0 & M_{\mathbf{k}}^{(bf)} \\ M_{\mathbf{k}}^{(ae)} & 0 & M_{\mathbf{k}}^{(ag)} & 0 & M_{\mathbf{k}}^{(aa)} & 0 & M_{\mathbf{k}}^{(ac)} & 0 \\ 0 & M_{\mathbf{k}}^{(bf)} & 0 & M_{\mathbf{k}}^{(bh)} & 0 & M_{\mathbf{k}}^{(bb)} & 0 & M_{\mathbf{k}}^{(bd)} \\ M_{\mathbf{k}}^{(ag)} & 0 & M_{\mathbf{k}}^{(ae)} & 0 & M_{\mathbf{k}}^{(ac)} & 0 & M_{\mathbf{k}}^{(aa)} & 0 \\ 0 & M_{\mathbf{k}}^{(bh)} & 0 & M_{\mathbf{k}}^{(bf)} & 0 & M_{\mathbf{k}}^{(bd)} & 0 & M_{\mathbf{k}}^{(bb)} \end{pmatrix}, \quad (6)$$

$$\begin{aligned} M_{\mathbf{k}}^{(aa)} &= 2J_{2b}S_1 \cos(k_x - k_y) + 2S_1(J_{5a} + J_{5b} - J_{2a} - J_{2b}), \\ M_{\mathbf{k}}^{(bb)} &= 2J_{2b}S_2 \cos(k_x - k_y) + 2S_2(J_{5a} + J_{5b} - J_{2a} - J_{2b}), \\ M_{\mathbf{k}}^{(ac)} &= -2J_{2a}S_1 \cos(k_x + k_y), \quad M_{\mathbf{k}}^{(bd)} = -2J_{2a}S_2 \cos(k_x + k_y), \\ M_{\mathbf{k}}^{(ae)} &= 2J_{5a}S_1 \cos(k_x - k_y), \quad M_{\mathbf{k}}^{(bf)} = 2J_{5a}S_2 \cos(k_x - k_y), \\ M_{\mathbf{k}}^{(ag)} &= -2J_{5b}S_1 \cos(k_x + k_y), \quad M_{\mathbf{k}}^{(bh)} = -2J_{5b}S_2 \cos(k_x + k_y). \end{aligned}$$

For the A_{1g} (LL) channel, $M_{\mathbf{k}} = \bar{K}_{\mathbf{k}}/2$ where $\bar{K}_{\mathbf{k}}$ is the same dynamical matrix $K_{\mathbf{k}}$ from Eq. (4) but with J_c set to zero.

To calculate the Raman response, we transform \mathcal{H}_{FL} into the magnon basis $\Phi'_{\mathbf{k}}$ using the Bogoliubov matrix $T_{\mathbf{k}}$ derived previously:

$$\mathcal{H}_{\text{FL}} = \sum_{\mathbf{k}} \Phi_{\mathbf{k}}^{\dagger} M_{\mathbf{k}} \Phi_{\mathbf{k}} = \sum_{\mathbf{k}} \Phi'^{\dagger}_{\mathbf{k}} M'_{\mathbf{k}} \Phi'_{\mathbf{k}}, \quad (7)$$

where $M'_{\mathbf{k}} = T_{\mathbf{k}}^{\dagger} M_{\mathbf{k}} T_{\mathbf{k}}$ is the Raman vertex in the magnon eigenbasis. The final expression Eq. (7) contains the density-like terms, the substitutional terms, and the 2M terms. A density-like term (e.g., $\alpha_{1,\mathbf{k}}^{\dagger} \alpha_{1,\mathbf{k}}$) generates an elastic response, and a substitutional term (e.g., $\alpha_{1,\mathbf{k}}^{\dagger} \alpha_{2,\mathbf{k}}$) replaces a thermally populated magnon with another magnon at same \mathbf{k} , which is suppressed exponentially $\sim \exp(-E_{2,\mathbf{k}}/k_B T)$ at low temperatures. The 2M terms (e.g., $\alpha_{1,\mathbf{k}}^{\dagger} \alpha_{5,-\mathbf{k}}^{\dagger}$) produce the dominant inelastic process at low temperatures. Therefore, only the 2M terms are retained in calculating the Raman response below.

The non-interacting 2M Raman spectrum ($\text{Im } \chi_0$) is calculated as a retarded linear response function expressed with the transformed matrix elements, $M'_{ij}(\mathbf{k}) = \langle \alpha_{i,\mathbf{k}}^{\dagger} \alpha_{j,-\mathbf{k}}^{\dagger} | \mathcal{H}_{\text{FL}} | 0 \rangle$:

$$\chi_0(\omega) = \frac{1}{N} \sum_{\mathbf{k},i,j} |M'_{ij}(\mathbf{k})|^2 (1 - e^{-E_{ij}(\mathbf{k})/k_B T}) \left(\frac{1}{\hbar\omega - E_{ij}(\mathbf{k}) + i\Gamma} - \frac{1}{\hbar\omega + E_{ij}(\mathbf{k}) + i\Gamma} \right). \quad (8)$$

Here, the sum is over all \mathbf{k} -points in the Brillouin zone and all pairs of magnon branches (i,j) . $E_{ij}(\mathbf{k}) = E_i(\mathbf{k}) + E_j(\mathbf{k})$ is the corresponding total 2M pair energy. For the numerical calculation, the summation was performed over a 2000×2000 \mathbf{k} -point mesh with a constant Lorentzian broadening ($\Gamma \equiv 1$ meV).

To account for magnon-magnon interactions J_{α} , we first define a reduced bare susceptibility $\bar{\chi}_0 = \chi_0 / \bar{M}$, which represents the intrinsic lineshape of the response, normalized by the mean-squared Raman vertex $\bar{M} = \frac{1}{N} \sum_{\mathbf{k},i,j} |M'_{ij}(\mathbf{k})|^2$. For the simple antiferromagnets, $\bar{\chi}_0$ is equivalent to the bare susceptibility calculated using the well-known dimensionless geometric form factors, such as $(\cos k_x - \cos k_y)^2$ for the B_{1g} channel [33,45]. The final interacting Raman response is then obtained via the RPA-type renormalization,

$$\text{Im } \chi_{\text{int}} = \text{Im} \frac{\chi_0}{1 + J_{\alpha} \cdot \bar{\chi}_0}. \quad (9)$$

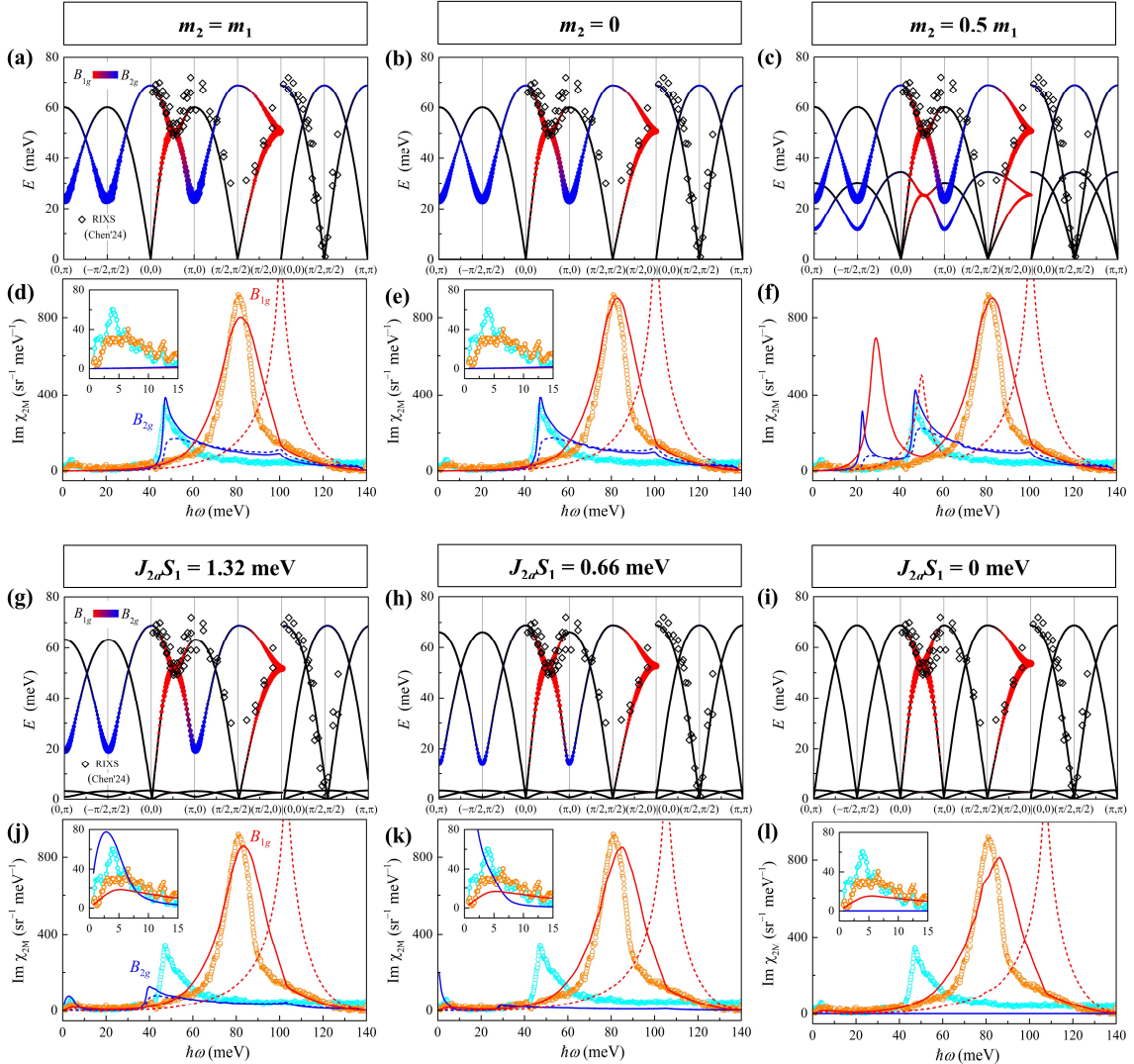


FIG. 13. Dependence of the 2M response on m_2 and J_{2a} . (a)-(f) Dependence of the 2M response on the low-moment m_2 . For these calculations, all exchange interactions are fixed to the values in Table I. The magnon band dispersion, the scattering matrix element strengths [(a)-(c)], and the corresponding B_{1g} and B_{2g} 2M Raman responses [(d)-(f)] are computed for different values of m_2 . If m_2 is zero (b) or made equal to m_1 (a), the low-energy features below 15 meV disappear from the calculated spectra [(d),(e) insets]. If m_2 is made comparable to m_1 (c), additional 2M features appear at a much higher energy range (f), inconsistent with the experimental data. (g)-(l) Calculation of the 2M Raman response when the diagonal exchange $J_{2a}S_1$ is set to values lower than 1.98 meV used in the main text (Table I). In these calculations, J_{2b} is fixed at half the value of J_{2a} , and $J_{3}S_1$ is adjusted to reproduce the magnon energies reported in the RIXS study [24]: 15 meV (g), 16 meV (h), 17 meV (i). The resulting spectra show that with decreasing J_{2a} , both the intensity and the energy of the B_{2g} 2M peak decrease and eventually vanish [(j)-(l)]. The colors, symbols, and line styles are identical to those in Figs. 3(b),(c).

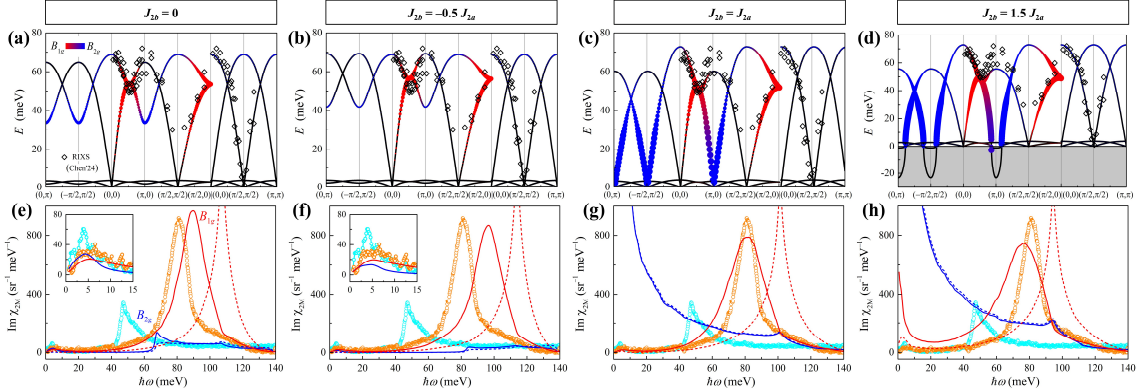


FIG. 14. Dependence of the 2M response on J_{2b} , the diagonal exchange within each magnetic sublattice. (a)-(d) Magnon band dispersion (solid lines) and corresponding scattering matrix element strengths (color intensity) for different values of J_{2b} . (e)-(h) The corresponding calculated B_{1g} and B_{2g} 2M Raman spectra, compared with the experimental data at 4.5 K. In these calculations, we use exchange and spin parameters given in Table I, while we slightly change J_3S_1 from 15 to 16 meV in (c) and (d) to better reproduce the reported magnon energies [24]. For zero and ferromagnetic J_{2b} [(a),(e) & (b),(g)], the B_{2g} mode is suppressed and shifted to higher energy, respectively. For larger antiferromagnetic J_{2b} [(c),(g) & (d),(h)], the B_{2g} mode gains intensity and moves to lower energy; for example, the energy becomes zero when $J_{2b} = J_{2a}$ [(c),(g)]. If J_{2b} exceeds J_{2a} , [(d),(h)], the magnetic structure becomes unstable, resulting in imaginary magnon energies.

To compare the final theoretical spectra with the experimental results, contributions arising from the high-spin (m_1) and low-spin (m_2) moments were scaled separately each with a single, common normalization factor applied to both the B_{1g} and B_{2g} channels. Supplementary calculations of the magnon dispersions and Raman spectra, obtained using parameters differing from the values in Table I, are presented in Figs. 13 and 14.

[1] H. Sun *et al.*, *Signatures of superconductivity near 80 K in a nickelate under high pressure*, *Nature* **621**, 493 (2023).

[2] K. Chen *et al.*, *Evidence of Spin Density Waves in $\text{La}_3\text{Ni}_2\text{O}_{7-\delta}$* , *Phys. Rev. Lett.* **132**, 256503 (2024).

[3] I. Plokhikh *et al.*, *Unraveling Spin Density Wave Order in Layered Nickelates $\text{La}_3\text{Ni}_2\text{O}_7$ and $\text{La}_2\text{PrNi}_2\text{O}_7$ via Neutron Diffraction*, arXiv:2503.05287.

[4] Y.-B. Liu *et al.*, *s^\pm -Wave Pairing and the Destructive Role of Apical-Oxygen Deficiencies in $\text{La}_3\text{Ni}_2\text{O}_7$ under Pressure*, *Phys. Rev. Lett.* **131**, 236002 (2023).

[5] H. Sakakibara *et al.*, *Possible High T_c Superconductivity in $\text{La}_3\text{Ni}_2\text{O}_7$ under High Pressure through Manifestation of a Nearly Half-Filled Bilayer Hubbard Model*, *Phys. Rev. Lett.* **132**,

106002 (2024).

- [6] Y. Zhang *et al.*, *Structural phase transition, s_{\pm} -wave pairing, and magnetic stripe order in bilayered superconductor $La_3Ni_2O_7$ under pressure*, Nat. Commun. **15**, 2470 (2024).
- [7] S. Ryee *et al.*, *Quenched Pair Breaking by Interlayer Correlations as a Key to Superconductivity in $La_3Ni_2O_7$* , Phys. Rev. Lett. **133**, 096002 (2024).
- [8] X.-Z. Qu *et al.*, *Bilayer t - J - J_{\perp} Model and Magnetically Mediated Pairing in the Pressurized Nickelate $La_3Ni_2O_7$* , Phys. Rev. Lett. **132**, 036502 (2024).
- [9] C. Lu *et al.*, *Interlayer-Coupling-Driven High-Temperature Superconductivity in $La_3Ni_2O_7$ under Pressure*, Phys. Rev. Lett. **132**, 146002 (2024).
- [10] R. Jiang *et al.*, *Pressure Driven Fractionalization of Ionic Spins Results in Cupratelike High- T_c Superconductivity in $La_3Ni_2O_7$* , Phys. Rev. Lett. **132**, 126503 (2024).
- [11] Q.-G. Yang *et al.*, *Possible s_{\pm} -wave superconductivity in $La_3Ni_2O_7$* , Phys. Rev. B **108**, L140505 (2023).
- [12] F. Lechermann *et al.*, *Electronic correlations and superconducting instability in $La_3Ni_2O_7$ under high pressure*, Phys. Rev. B **108**, L201121 (2023).
- [13] Z. Fan *et al.*, *Superconductivity in nickelate and cuprate superconductors with strong bilayer coupling*, Phys. Rev. B **110**, 024514 (2024).
- [14] G. Heier *et al.*, *Competing d_{xy} and s_{\pm} pairing symmetries in superconducting $La_3Ni_2O_7$: LDA + FLEX calculations*, Phys. Rev. B **109**, 104508 (2024).
- [15] J. Chen *et al.*, *Orbital-selective superconductivity in the pressurized bilayer nickelate $La_3Ni_2O_7$: An infinite projected entangled-pair state study*, Phys. Rev. B **110**, L041111 (2024).
- [16] M. Bejas *et al.*, *Out-of-plane bond-order phase, superconductivity, and their competition in the t - J_{\parallel} - J_{\perp} model: Possible implications for bilayer nickelates*, Phys. Rev. B **111**, 144514 (2025).
- [17] W. Xi *et al.*, *Transition from s_{\pm} -wave to $d_{x^2-y^2}$ -wave superconductivity driven by interlayer interaction in the bilayer two-orbital model of $La_3Ni_2O_7$* , Phys. Rev. B **111**, 104505 (2025).
- [18] Y.-Q. Liu *et al.*, *Variational quantum Monte Carlo investigations of the superconducting pairing in $La_3Ni_2O_7$* , Phys. Rev. B **112**, 014511 (2025).
- [19] L. B. Braz *et al.*, *Interlayer interactions in $La_3Ni_2O_7$ under pressure: From s_{\pm} to d_{xy} -wave superconductivity*, Phys. Rev. Research **7**, 033023 (2025).
- [20] Z. Luo *et al.*, *High- T_c superconductivity in $La_3Ni_2O_7$ based on the bilayer two-orbital t - J model*, npj Quantum Mater. **9**, 61 (2024).
- [21] J. Guo *et al.*, *Revealing superconducting gap in $La_3Ni_2O_{7-\delta}$ by Andreev reflection spectroscopy under high pressure*, arXiv.2509.12601.
- [22] Z.-Y. Cao *et al.*, *Direct Observation of d -Wave Superconducting Gap Symmetry in Pressurized $La_3Ni_2O_{7-\delta}$ Single Crystals*, arXiv.2509.12606.
- [23] S. Fan *et al.*, *Superconducting gap structure and bosonic mode in $La_2PrNi_2O_7$ thin films at ambient pressure*, arXiv.2506.01788.
- [24] X. Chen *et al.*, *Electronic and magnetic excitations in $La_3Ni_2O_7$* , Nat. Commun. **15**, 9597 (2024).
- [25] T. Xie *et al.*, *Strong interlayer magnetic exchange coupling in $La_3Ni_2O_{7-\delta}$ revealed by inelastic neutron scattering*, Sci. Bull. **69**, 3221 (2024).
- [26] R. Khasanov *et al.*, *Pressure-enhanced splitting of density wave transitions in $La_3Ni_2O_{7-\delta}$* , Nat. Phys. **21**, 430 (2025).
- [27] N. K. Gupta *et al.*, *Anisotropic spin stripe domains in bilayer $La_3Ni_2O_7$* , Nat. Commun. **16**, 6560 (2025).

[28] D. Zhao *et al.*, *Pressure-enhanced spin-density-wave transition in double-layer nickelate $La_3Ni_2O_{7-\delta}$* , *Sci. Bull.* **70**, 1239 (2025).

[29] J. Luo *et al.*, *Microscopic Evidence of Charge- and Spin Density Waves in $La_3Ni_2O_{7-\delta}$ Revealed by ^{139}La -NQR*, *Chinese Phys. Lett.* **42**, 067402 (2025).

[30] P. A. Fleury and R. Loudon, *Scattering of Light by One- and Two-Magnon Excitations*, *Phys. Rev.* **166**, 514 (1968).

[31] P. A. Fleury, *Evidence for Magnon-Magnon Interactions in $RbMnF_3$* , *Phys. Rev. Lett.* **21**, 151 (1968).

[32] P. A. Fleury and H. J. Guggenheim, *Magnon-Pair Modes in Two Dimensions*, *Phys. Rev. Lett.* **24**, 1346 (1970).

[33] W. J. Brya and P. M. Richards, *Frequency moments for two-spin light scattering in antiferromagnets*, *Phys. Rev. B* **9** 2244 (1973).

[34] W. J. Brya *et al.*, *Frequency Moments of Magnetic Light Scattering in NiF_2* , *AIP Conf. Proc.* **10**, 729 (1973).

[35] D. J. Lockwood and M. H. Cottam, *Light scattering from magnons in MnF_2* , *Phys. Rev. B* **35**, 1973 (1987).

[36] R. R. P. Singh *et al.*, *Quantitative Determination of Quantum Fluctuations in the Spin-1/2 Planar Antiferromagnet*, *Phys. Rev. Lett.* **62**, 2736 (1989).

[37] P. E. Sulewski *et al.*, *Observation of Chiral Spin Fluctuations in Insulating Planar Cuprates*, *Phys. Rev. Lett.* **67**, 3864 (1991).

[38] K.-Y. Choi *et al.*, *Anomalous orbital dynamics in $LaSrMnO_4$ observed by Raman spectroscopy*, *Phys. Rev. B* **77**, 064415 (2008).

[39] S. Li *et al.*, *Symmetry-Resolved Two-Magnon Excitations in a Strong Spin-Orbit-Coupled Bilayer Antiferromagnet*, *Phys. Rev. Lett.* **125**, 087202 (2020).

[40] S. Sugai *et al.*, *Carrier-density-dependent momentum shift of the coherent peak and the LO phonon mode in p-type high- T_c superconductors*, *Phys. Rev. B* **68**, 184504 (2003).

[41] Y. Onose *et al.*, *Charge dynamics in underdoped $Nd_{2-x}Ce_xCuO_4$: Pseudogap and related phenomena*, *Phys. Rev. B* **69**, 024504 (2004).

[42] D.-H. Gim *et al.*, *Orbital-Selective Quasiparticle Depletion across the Density Wave Transition in Trilayer Nickelate $La_4Ni_3O_{10}$* , *Phys. Rev. Lett.* **135**, 136505 (2025).

[43] S. Sugai *et al.*, *Superconducting pairing and the pseudogap in the nematic dynamical stripe phase of $La_{2-x}Sr_xCuO_4$* , *J. Phys.: Condens. Matter* **25**, 475701 (2013).

[44] R. J. Elliott *et al.*, *Magnon-Magnon and Exciton-Magnon Interaction Effects on Antiferromagnetic Spectra*, *Phys. Rev. Lett.* **21**, 147 (1968).

[45] R. J. Elliott and M. F. Thorpe, *The effects of magnon-magnon interaction on the two-magnon spectra of antiferromagnets*, *J. Phys. C: Solid State Phys.* **2**, 1630 (1969).

[46] H. LaBollita *et al.*, *Assessing spin-density wave formation in $La_3Ni_2O_7$ from electronic structure calculations*, *Phys. Rev. Mater.* **8**, L111801 (2024).

[47] C. Piamonteze *et al.*, *Spin-orbit-induced mixed-spin ground state in $RNiO_3$ perovskites probed by x-ray absorption spectroscopy: Insight into the metal-to-insulator transition*, *Phys. Rev. B* **71**, 020406(R) (2005).

[48] B. Zhang *et al.*, *Spin-charge-orbital order in nickelate superconductors*, *Phys. Rev. B*, **111**, 184401 (2025).

[49] D. K. Morr *et al.*, *Raman scattering in a two-layer antiferromagnet*, *Phys. Rev. B* **54**, 3468 (1996).